STUDIES ON THE NATURE OF FIELD EMISSION SITES*

D. MOFFAT, P. BARNES, T. FLYNN, J. GRABER, L. HAND, W. HARTUNG,
T. HAYES, J. KIRCHGESSNER, J. KNOBLOCH, R. NOER†, H. PADAMSEE,
D. RUBIN AND J. SEARS

Laboratory of Nuclear Studies, Cornell University, Ithaca, NY 14853-5001

ABSTRACT

A specially designed superconducting niobium RF cavity has supported a cw surface electric field of 145 MV/m [1], while a superconducting RFQ has reached the record pulsed field of 210 MV/m [2]. One of the reasons that such phenomenal performances are not achieved in typical accelerating cavities is that field emission absorbs the available RF power. Field emission scanning microscopy (FESM) has indicated that particulates are a source of emission on broad-area niobium DC cathodes [e.g. 3, 4]. Temperature and x-ray maps have been used to locate emitters in RF cavities and to investigate their field dependence. The gap between the RF and DC work was that there had been no direct observation of field emitters or emission sites in cavities. The present study attempts to bridge this gap and offers the first look at the surface of a niobium RF cavity after field emission processing.

INTRODUCTION

Field emission of electrons occurs when electrons tunnel through the quantum mechanical barrier at the surface of a metal. This process is depicted in Figure 1. There are several theories concerning the mechanism of emission, but the equation most commonly used to describe field emission in RF cavities is that based on the work of Fowler and Nordheim [5–8]. The Fowler-Nordheim equation, which correctly describes DC field emission for the case of a pointed electrode and opposing planar surface, suggests that field emission currents should not be significant, i.e. ≤ 1 A/cm^2, for surface fields below ~1900 MV/m. In practice, however, field

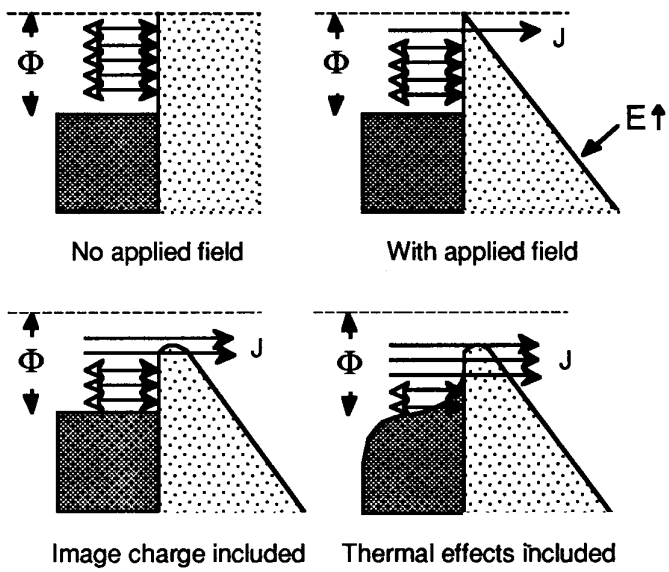

Figure 1 Schematics of the quantum mechanical barrier at the surface of a metal through which electrons may tunnel. Φ is the work function, E is the applied electric field and J is the emitted current density.

* Work supported by the National Science Foundation and the US-Japan collaboration
† Present address: Carleton College, Northfield, MN 55057

emission loading of cavities has been observed at fields as low as ~5 MV/m. To reconcile this disparity, a field enhancement factor, β, is used. (Other parameters in the F-N equation, e.g. the work function ϕ [9], could be adjusted to account for the observed emission currents. Alternatively, another theory could be applied.) Thus, one approach to reduce the field emission loading in a cavity, is to understand the origin of β and learn how to reduce it.

To elicit details of the field emission process in superconducting RF cavities, several indirect visualization techniques have been developed. Temperature and x-ray mapping have yielded much information regarding the location of emitters and the field dependence of emission. Figure 2 shows a typical temperature map of a cavity before and after the destruction of an emitter. (When an emitter is detroyed, it is said to have been processed.) Cavity mapping, while not providing any microscopic information about actual emitters, has led the development of techniques which are effective in reducing field emission loading at the field levels typical of present applications.

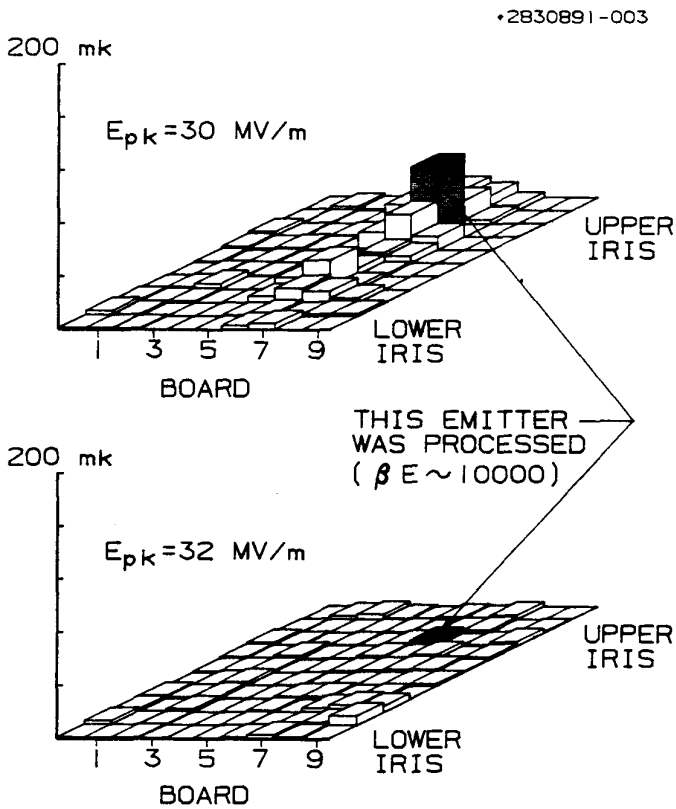

Figure 2 Temperature maps from a 3 GHz S-band cavity test showing the processing of an emitter.

Particle accelerators being proposed for the near future, e.g. CESR-B and TeSLA, require superconducting RF cavities capable of supporting surface fields two to five times higher than those in present accelerator cavities. To achieve this reproducibly and economically will require more detailed information about actual emitters and an improved understanding of what constitutes processing. This information may be acquired only by microscopic examination of the RF surfaces of niobium cavities.

INVESTIGATIONS OF EMISSION SITES ON NIOBIUM RF SURFACES

At Cornell we have developed a superconducting cavity, called the "mushroom" cavity, in which a small region is exposed to very high surface RF electric fields. This region, the "dimple", is part of a demountable niobium end-plate which fits into our scanning electron microscope (SEM). A detailed description of this cavity can be found in [1]. A similar cavity is undergoing testing and development at Saclay [10]. To complement and corroborate the discoveries made using the mushroom cavity, three S-band cavities have also been subjected to high surface electric fields and then cut open for SEM examination. Cross-sectional views of the mushroom and S-band cavities and their surface fields are shown in Figures 3 and 4, respectively. A rudimentary DC field emission apparatus was assembled to supplement the RF field emission studies.

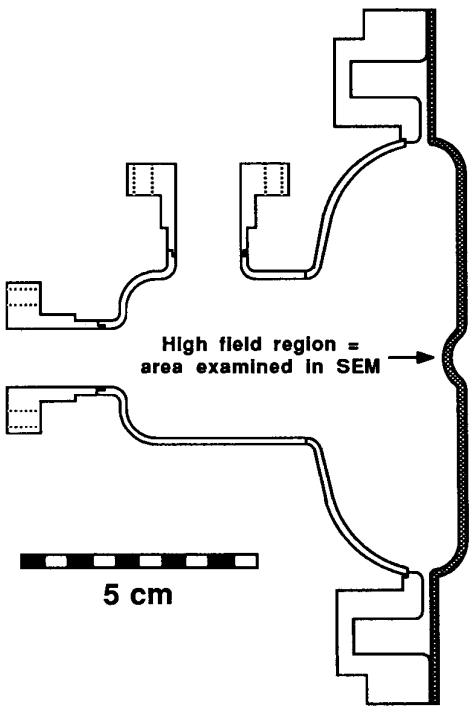

Figure 3a Cross-sectional view of the "mushroom" cavity. This cavity was tested in this orientation in the TM_{020} mode, the frequency of which is ~6 GHz. The entire end-plate (shaded) can be removed and placed in the SEM for examination.

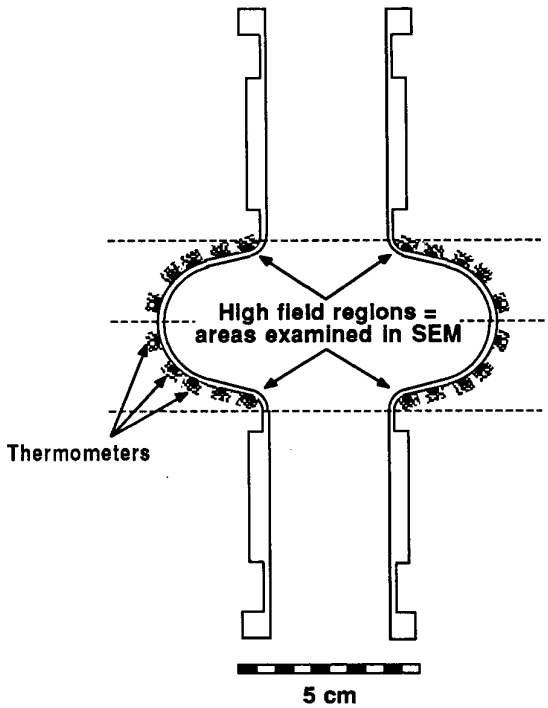

Figure 3b Cross-sectional view of the 3 GHz S-band cavity showing the azimuthal positions of the thermometers. The cavities are tested in this orientation in the TM_{010} mode. The cavities were cut on the dotted lines for SEM examination.

Tests involving the mushroom cavity began with measuring the cavity Q_o at 4.2K, and then lowering the bath temperature to ~1.5K. After processing a multipacting barrier at 2-10 MV/m, the RF power was increased incrementally, usually to the point of breakdown. Some tests were stopped in an attempt to correlate the number of spots seen with the peak field. The transmitted power coupler doubled as an emitted current collector, but it was found that there was a significant contribution to the current by secondary and higher-order electrons. Field emission loading was observed as a drop in Q_o and as collected current. A representative Q_o vs E_{pk} curve for this cavity is shown in Figure 5.

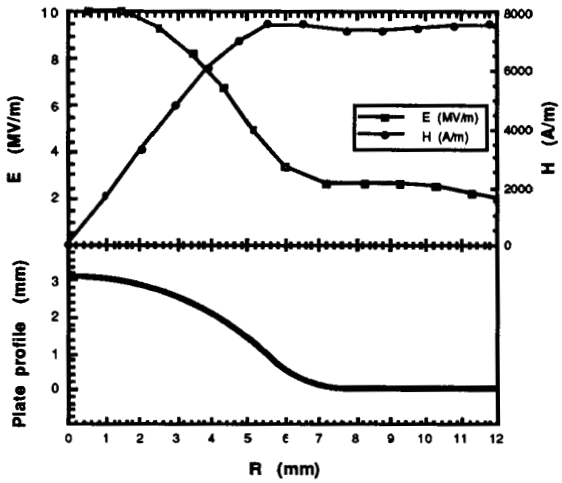

Figure 4a Surface electric and magnetic fields on the mushroom cavity dimple.

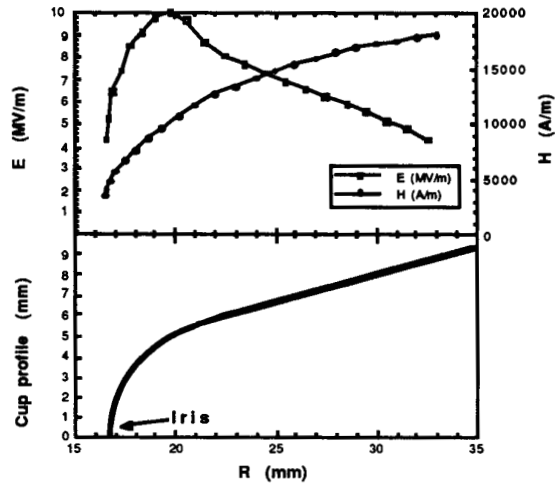

Figure 4b Surface electric and magnetic fields in the 3 GHz S-band cavity.

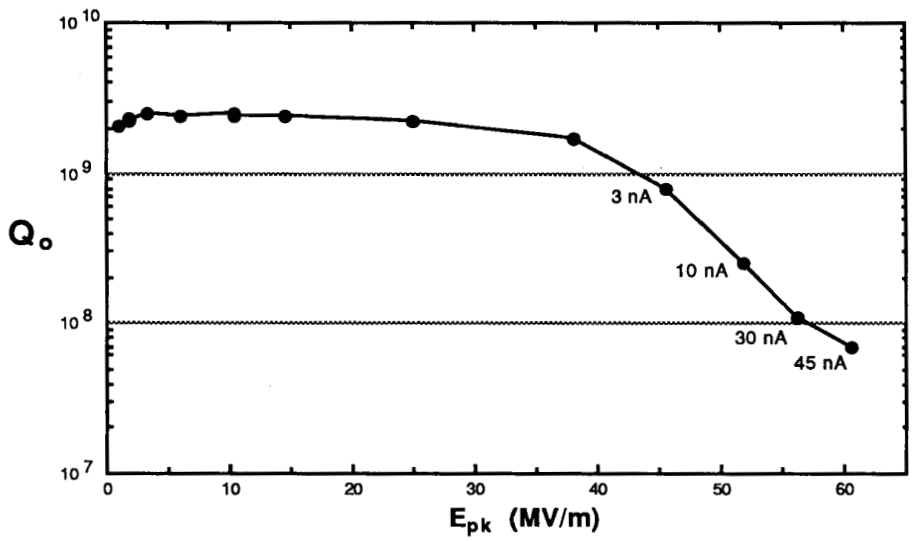

Figure 5 A representative Q_o vs E_{pk} curve from a mushroom cavity test. Collected current values are indicated.

The S-band cavities examined were part of a study on high peak power pulsed processing [11, 12]. After measuring the Q_o at 4.2K, the bath temperature was lowered to ~1.5K. A Q_o vs E_{pk} curve was then obtained up to an input power level of ~20 W. HPP processing at a fixed power level was then performed. When the field emission, or breakdown behavior, appeared to be stable, another low power Q_o vs E_{pk} curve was obtained. This process was repeated with increased power during HPP until no further reduction of field emission at low power was observed, or until thermal breakdown was encountered.

Particulates on a surface have been clearly identified in the DC literature as a source of field emission [3, 4]. Therefore, it is desired that cavity preparation procedures create and maintain a particulate-free surface. Two SEM micrographs of clean niobium are shown in Figure 6. The grain structure observed is the result of acid

treatment with buffered chemical polish (BCP). All RF surfaces that we examined before testing had a similar appearance. No particulates are readily visible, though it must be noted that identifying micron and submicron-sized particles over broad areas is difficult and time-consuming. While every attempt was made to maintain a particulate-free surface while the cavities were being attached to the test-stands, it will be shown below that apparently we were not always successful.

SEM examinations of the RF surfaces of these cavities after testing revealed features that were completely unexpected. These features, which were associated with field emission activity, are discussed below in order of their size. The discussion begins with the larger features and proceeds to the smaller.

Starbursts

Figure 7 is a collage of micrographs of a mushroom dimple that reached a peak field of 66 MV/m. Distributed randomly over the dimple surface are ~30 "starburst" shaped regions. The number of starburst regions seen on a given plate varied with the maximum surface field reached and the surface treatment given the end-plate. Examples of individual starbursts seen in the mushroom cavity are shown in Figure 8; starbursts from the S-band cavity are shown in Figure 9. The starbursts from the mushroom cavity, which was operated at ~6 GHz, are ~100 μm in diameter while those from the S-band cavities, which were operated at 3 GHz, are ~200 μm in diameter. The remnants of what is believed to have been an emitter were usually found at the center of each starburst.

Each starburst is a region of reduced secondary electron emission coefficient. While a specific cause for this is not known, possible explanations include: 1) the surface oxide layer was etched away by a plasma created during emitter processing; 2) a residual surface hydrocarbon layer was cracked by an arc/plasma during processing; 3) a spray of niobium caused by the vaporization of the emitter coating the surface. Energy dispersive x-ray spectroscopy (EDS) analyses in the SEM indicated no foreign elements or increase in the concentration of oxygen or carbon in the starbursts, although it must be remembered that a thin surface film is very difficult, if not impossible, to analyze. (Detection of carbon with our EDS system is made possible by removing the beryllium window.) It was observed that upon exposure to air, these starbursts faded over the period of many hours. This suggests an oxidation process. Because of this sensitivity to atmospheric exposure, mushroom end-plates have not been examined with an optical microscope. (Apparently, features such as these starbursts were observed in the late 1700's by Professor Lichtenberg at the University of Göttingen [13].)

Figure 10 shows a starburst that was created in our DC apparatus on a niobium cathode. This starburst occurred not at a site of strong field emission, but rather at a site which sparked at 110 MV/m with a current of only 12 nA. A starburst was also found at another site which sparked at 90 MV/m and 15,000 nA. Other sites which did not spark, even though the field emission currents were on the order of 1000 nA at 120 MV/m, left no trace on the niobium surface.

Tracking

In the mushroom cavity we have observed several times "tracks" emanating from the starbursts. Two examples are shown in Figure 11. These tracks usually change direction sharply, as in Figure 11a, but smooth arcs have also been seen.

Craters of Molten Niobium

Undoubtably, the most dramatic and surprising feature we have seen are craters of molten niobium, which were found at the centers of starbursts. The observation that small regions of the surface of a cavity in 1.5K helium could exceed 2740K was completely unexpected. Examples of craters from the mushroom cavity are shown in Figure 12, S-band examples in Figure 13. Using EDS, we found that many crater fields contained only niobium, i.e. no foreign elements. It should be noted that most, but not all, of the starbursts contained crater fields.

Craters have been seen in two different groupings: clustered and overlapped. Individual craters in each grouping are typically ~1-4 μm in diameter, although craters as small as ~.5 μm are common. When craters are overlapped, they usually appear as a tight ensemble about a central point (ensembles as large as ~20 μm have been seen). Occasionally, each successively formed crater is offset from the previous one, forming a path of overlapped craters.

The heavily overlapped sites appear to have a central column of niobium rising from them. Tilting the end-plate in the SEM reveals that there is actually very little surface relief (Figure 14).

Returning to the DC starburst shown in Figure 10, several craters of molten niobium can be seen. Again, such features were observed only at the sites which sparked.

Ripple Patterns

The most curious feature we have seen are the ripples, or rings, concentrically surrounding some of the craters. These ripples, seen in Figures 15 and 16, extend for several tens of microns from the cratered region. The spacing of the ripples varied about a factor of two within each site and from site to site. The ripples seen on mushroom cavity end-plates had a spacing of ~.15-.25 μm, while those seen on S-band cavity cups had a spacing of ~.3-.5 μm. Even though the spacings varied over a range of values, the spacings observed in the mushroom cavity, which was operated at ~6 GHz, were about a factor of two smaller than those observed in the S-band cavities, which were operated at 3 GHz. Not all cratered regions contained ripples, but whenever there were ripples, they emanated from craters. Several instances have been documented where there were no ripples, but rather broken rings or nodules (Figure 17).

The dimple containing the rings shown in Figure 15 was carefully removed from its end-plate and inserted in a scanning Auger microscope. The ripples did not disappear during the atmospheric exposure. Auger analysis did not reveal any elements heavier than helium in either the ripples or the spaces between them. (As is always the case, oxygen and carbon were found, but no real difference between the rippled surface and the background was discernable.) This dimple is presently being examined in a scanning tunneling microscope for measurement of the surface relief.

The origin of these ripples is uncertain. The extreme periodicity of their spacing would seem to indicate that an entire pattern was created, or frozen in place, at one instant in time. In support of this supposition is the fact that where a pattern encounters a discontinuity, the ripples match perfectly on each side. There would also appear to be some dependence of ripple spacing on RF frequency.

Particles of Foreign Elements

Approximately half of the starbursts seen in the S-band cavities were found to contain foreign elements. This percentage was much lower in the mushroom cavity. Usually the foreign element(s) were found in a particle(s) close to the center of a starburst. The morphology of these particles indicates that they had been partially or fully melted. Below is a summary of the foreign elements found, discussed in order of decreasing frequency.

Iron/stainless steel Figure 18a shows several rounded particles of stainless steel very near a niobium crater on a mushroom dimple, and a faint starburst is also visible. (Stainless steel is differentiated from iron by the concomitant detection of nickel and/or chromium.) Figure 18b shows a stainless steel particle found at another site in the mushroom cavity. The ends of this particle are rounded, which suggests that they had been heated to the melting point and spherodized. A small cluster of craters can be seen just above this particle. The features indicated in Figure 19a were found to contain iron. There are no identifiable particles in Figure 19b; nevertheless, the edges of the crater were found to contain iron and chromium. The fine nodules surrounding this crater were too small for EDS analysis. (The micrographs in Figure 19 were taken from S-band cavities.) The source of the iron/steel may have been particles which fell into a cavity from the bolts, flanges and tools used to attach it to a test stand. Alternatively, particles of iron/steel may have been rolled deep into the niobium during sheet fabrication and then exposed during BCP treatment.

Indium Striking photographs showing the remnants of indium contamination were obtained after one S-band cavity test. Figure 20 shows the splashed remains of two indium particles. These remnants were found at the centers of starbursts. Figure 21 shows a partially melted flake of indium, ~11 μm long. The niobium surface around this flake is covered with a very fine "dust". The "dust" particles are ≤ .1 μm in diameter, making EDS analysis impossible. It is reasonable to believe that the features shown in Figure 20 were created when a flake such as the one shown in Figure 21 completely melted. There is no starburst around the flake shown in Figure 21.

Almost all cavity seals are made with indium O-rings. There is some concern that the process of compressing indium wire between flanges produces indium dust which may settle on the cavity surface. While there is evidence to indicate that there is dust in cavity test stands [14], it is unclear that it may be attributed to the indium seals. On the other hand, it is clear that indium particles may fall into a cavity when an old O-ring is scraped off. The latter is thought to be the more probable source, especially when the fact that copper particles are often found in conjunction with indium is considered (see next section). It was believed that treating the cavity with BCP after indium seal removal would dissolve any indium particles; it turns out that indium is attacked by BCP too slowly to be practically useful. For this reason, a soak in nitric acid, HNO_3, is now performed prior to any treatment given a cavity that is to be retested. This precaution has already been implemented at other laboratories [10, 15].

Copper Particles of copper have been found in both the mushroom and S-band cavities (Figure 22). Usually they appeared in asociation with indium particles. The most probable source of copper is the indium scraper. It is possible, but improbable, that copper dust may have come from our threaded RF couplers.

Titanium Small spheres of titanium were discovered on one dimple (Figure 23). Possible sources of titanium are inclusions in the niobium sheet, or vapors from the ion pump.

Teflon In one of the first tests of the mushroom cavity a particle of teflon was found about half way down the side of the dimple. This particle, shown in Figure 24, appears to have partially melted and vaporized. There was no starburst associated with this particle, although the end-plate may have been exposed to air too long prior to SEM examination. It is not clear if this particle was responsible for the observed emission, or if it simply heated in the high RF electric field. The highest field at this particle was ~40 MV/m. This particle most likely came from the indium O-ring former.

Other elements Infrequently, traces of sodium, magnesium, aluminum, silicon, chlorine and calcium were found. These elements were associated with small, nondescript particles. Possible sources are either particulates in our water, or dust.

ASSOCIATION WITH ELECTRON FIELD EMISSION

It was important to verify that the aforementioned features revealed the location of emission activity. Carbon from a pencil has been shown to be a reliable source of emission [16]. A fine-point pencil was lightly touched to an end-plate very close to the center of the dimple. Unfortunately, it was not possible to produce a single carbon flake, but rather hundreds of flakes were deposited over a ~200 μm diameter area. This end-plate was then tested and examined several times, the peak field increasing with each successive test.

It was found that RF processing caused the emission to decrease in intensity. As the peak field was increased, the number of carbon flakes remaining on the surface diminished dramatically and the number of molten niobium craters increased. This suggests that emitter processing leads to the formation of craters in the niobium surface. Two micrographs are shown in Figure 25. The micrograph in Figure 25a was taken after the peak field had been raised to 25 MV/m. Many carbon flakes can be seen, as well as much tracking and a starburst or two. The micrograph in Figure 25b was taken after the peak field had been increased to 60 MV/m. By matching the grains in the two micrographs, it can be seen that Figure 25b is an enlargement of the area shown in Figure 25a. Only a couple of carbon flakes can be seen in Figure 25b and the surface is covered with craters. It was interesting to find that the craters were carbon-free, indicating that light element particulates may vaporize completely.

This series of tests indicated that the craters found on a dimple occurred at, or extremely close to, sites of emission. What remains uncertain is whether any of these sites of former emission activity are still emission sites.

(The text will continue after the SEM micrographs.)

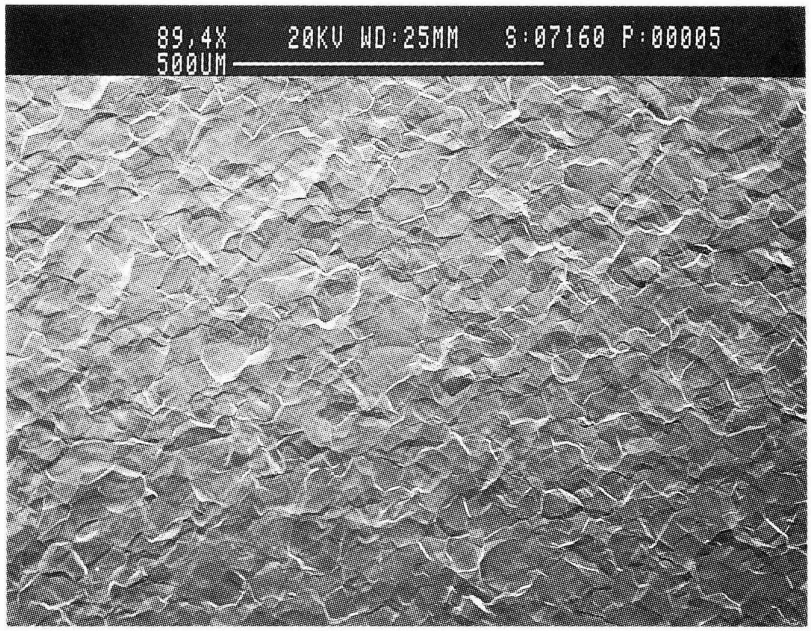

Figure 6a Low magnification SEM micrograph of a clean niobium surface. The grains are visible because of treatment with 1:1:1 BCP.

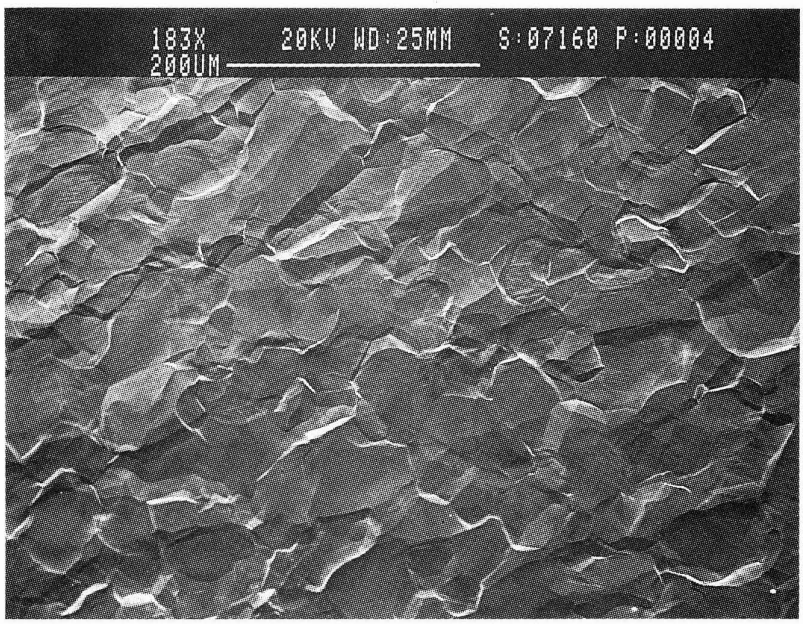

Figure 6b Higher magnification SEM micrograph of a clean niobium surface. The grains are visible because of treatment with 1:1:1 BCP.

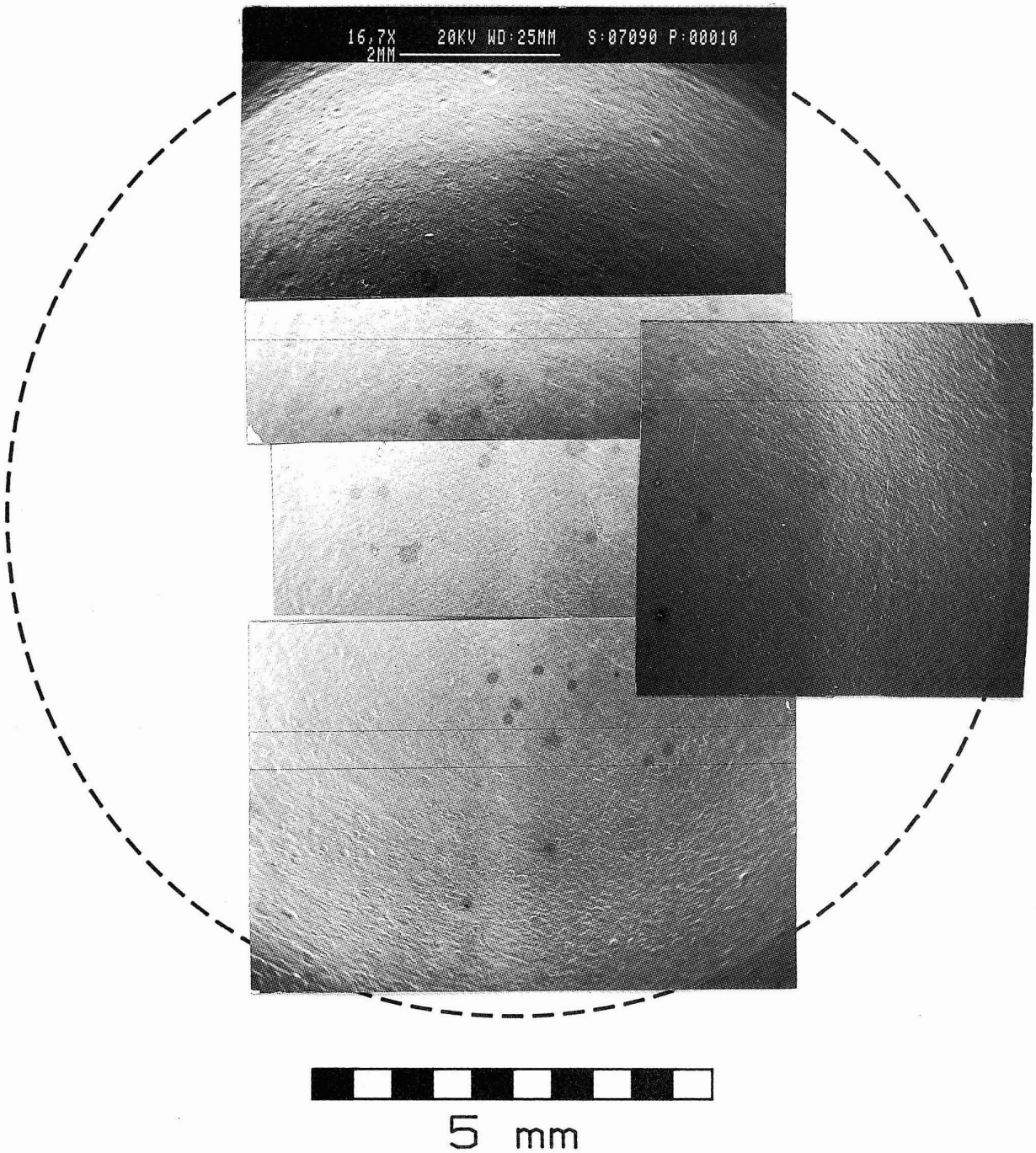

Figure 7 Collage of SEM micrographs of a mushroom dimple after RF testing. The peak field reached was 66 MV/m. Thirty starbursts can be seen. The dotted boundary indicates the perimeter of the dimple.

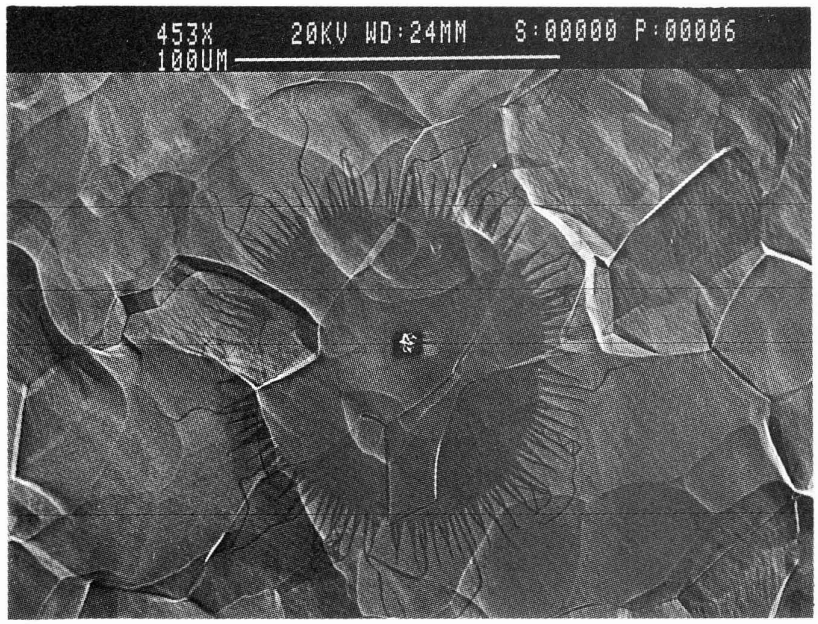

Figure 8a SEM micrograph of a starburst on a mushroom cavity dimple.

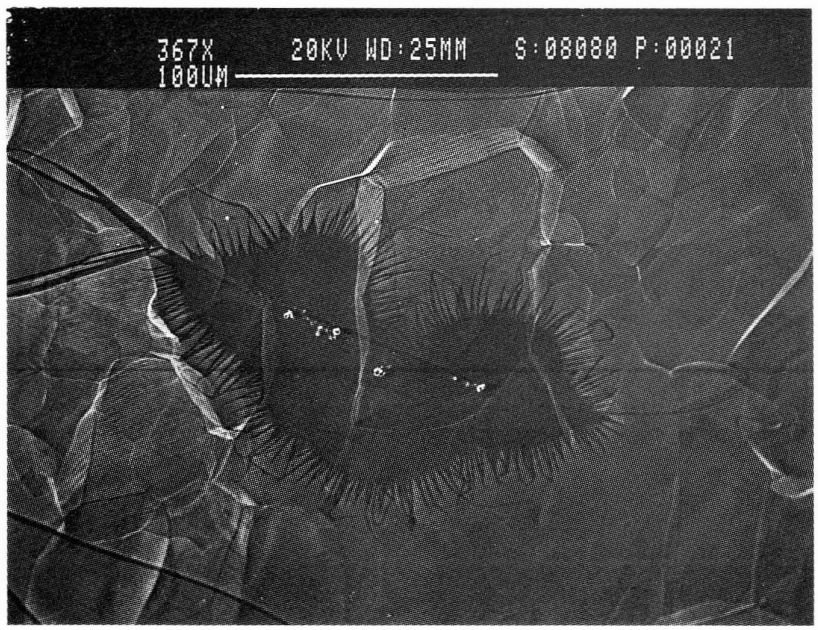

Figure 8b SEM micrograph of a multiple starburst on a mushroom cavity dimple.

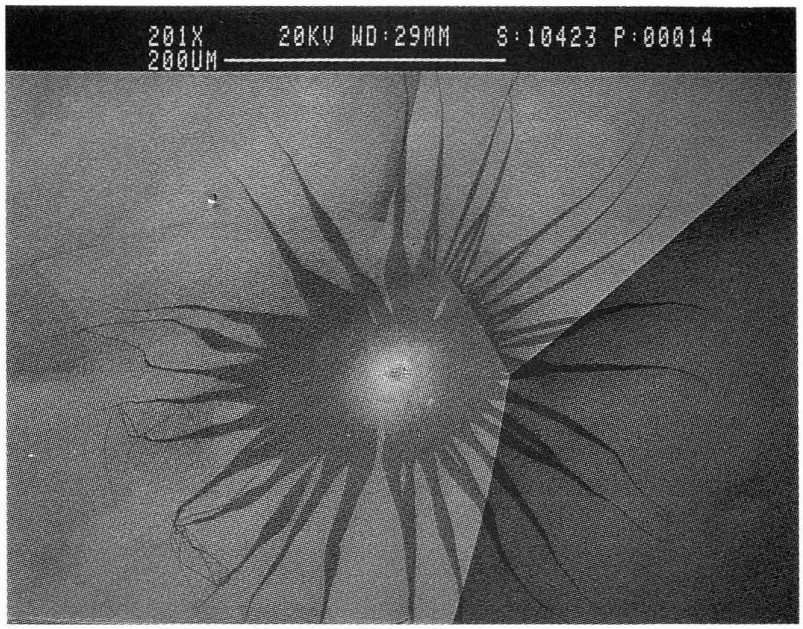

Figure 9a SEM micrograph of a starburst on a 3 GHz S-band cavity.

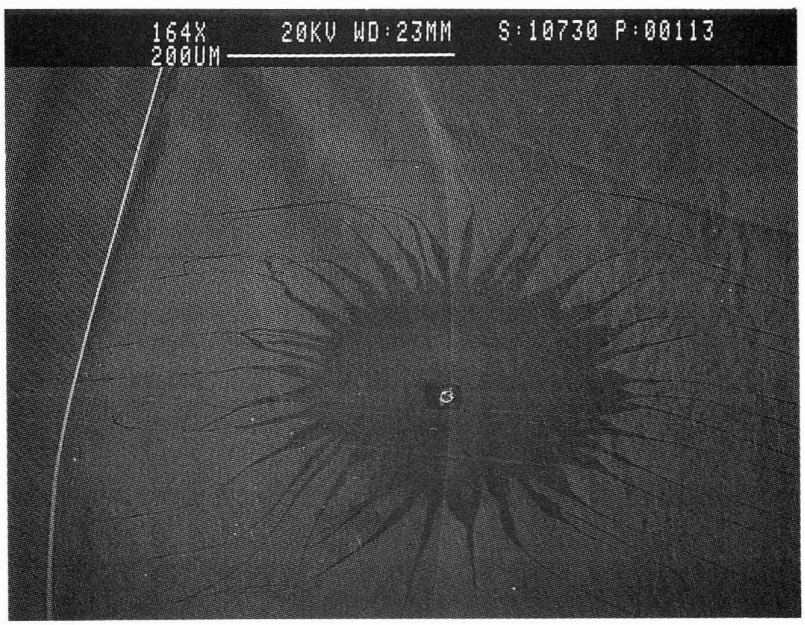

Figure 9b SEM micrograph of a starburst on a 3 GHz S-band cavity.

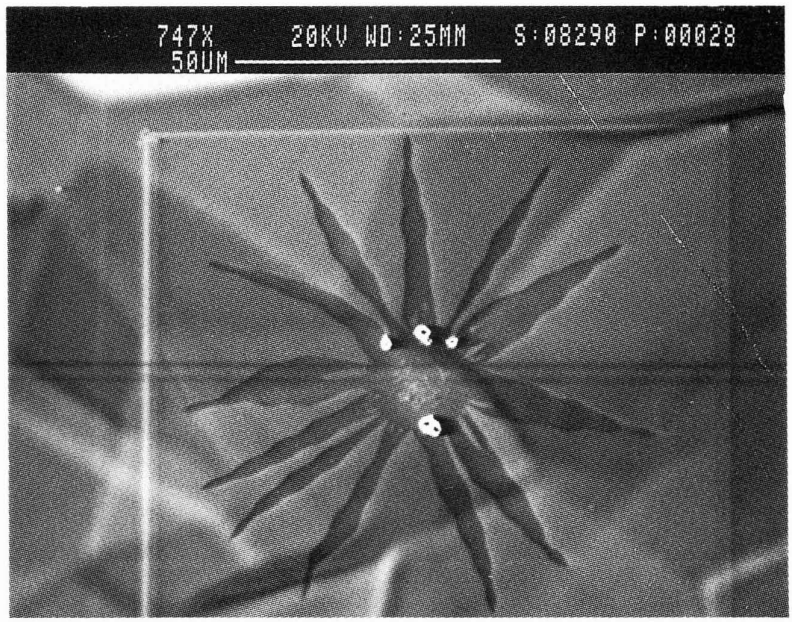

Figure 10 SEM micrograph of a starburst on a DC field emission cathode. This starburst was found at a site that sparked at 110 MV/m, even though the field emission current was very low, only 12 nA.

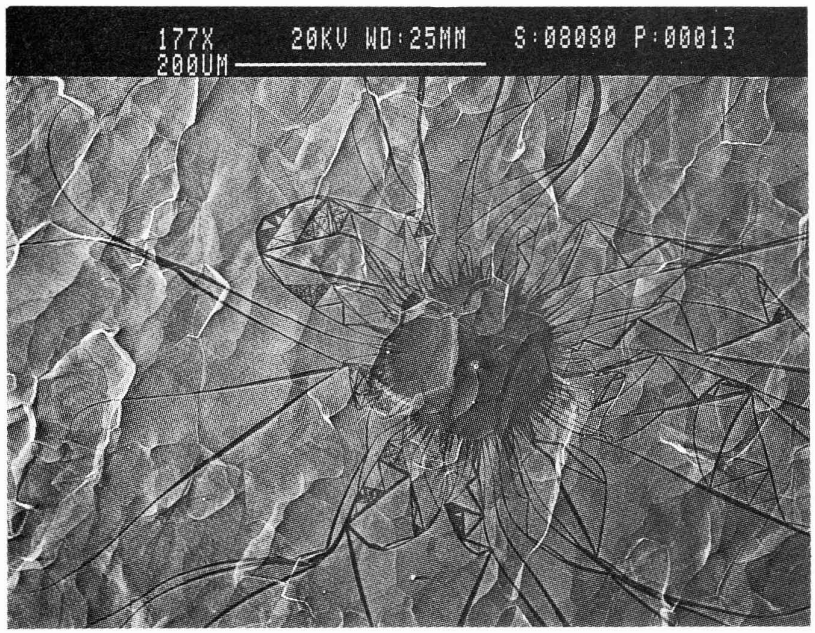

Figure 11a SEM micrograph of a dimple tested in the mushroom cavity showing the tracking phenomenon. Note the sharp angles of some of the branches.

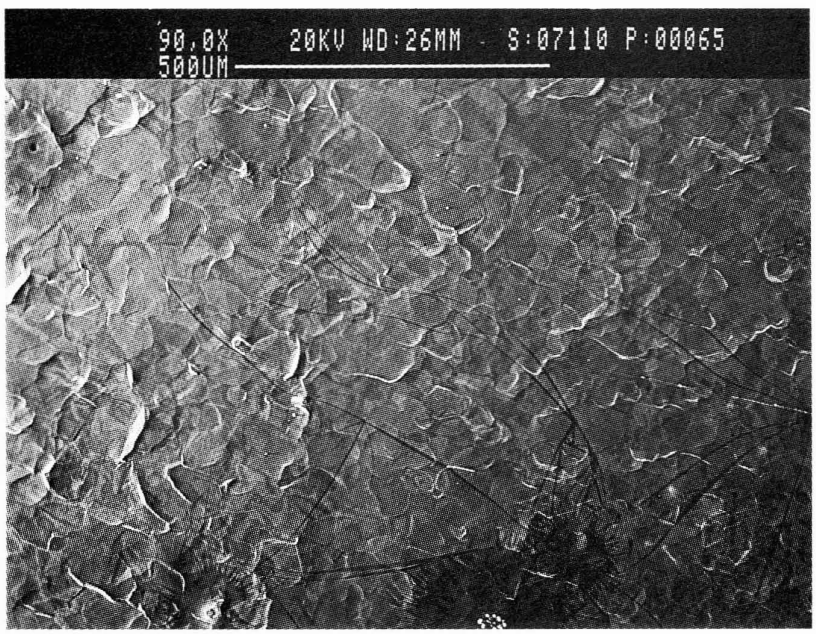

Figure 11b SEM micrograph of a dimple tested in the mushroom cavity showing the tracking phenomenon. The tracks in this micrograph can be seen to extend over 500 μm.

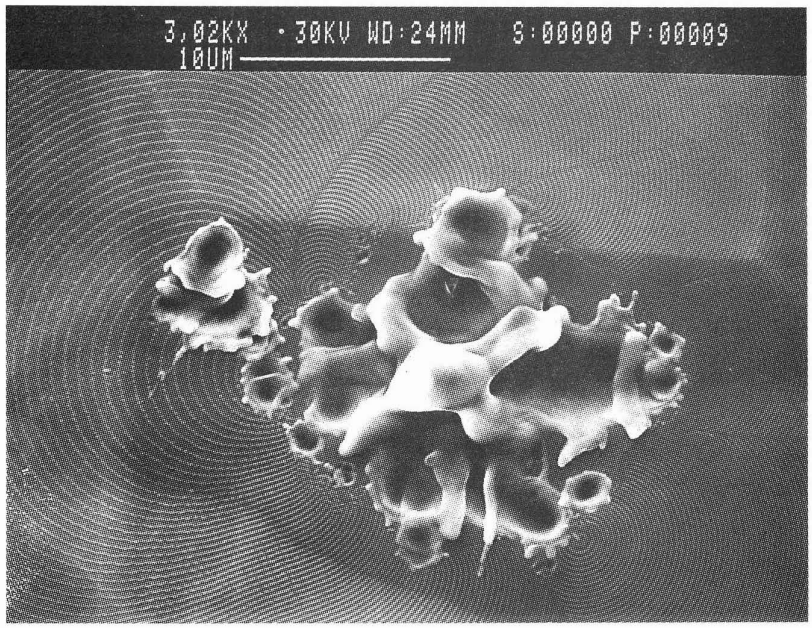

Figure 12a SEM micrograph of a dimple tested in the mushroom cavity showing overlapped craters of molten niobium. A higher magnification micrograph of the ripple pattern is shown in Figure 15.

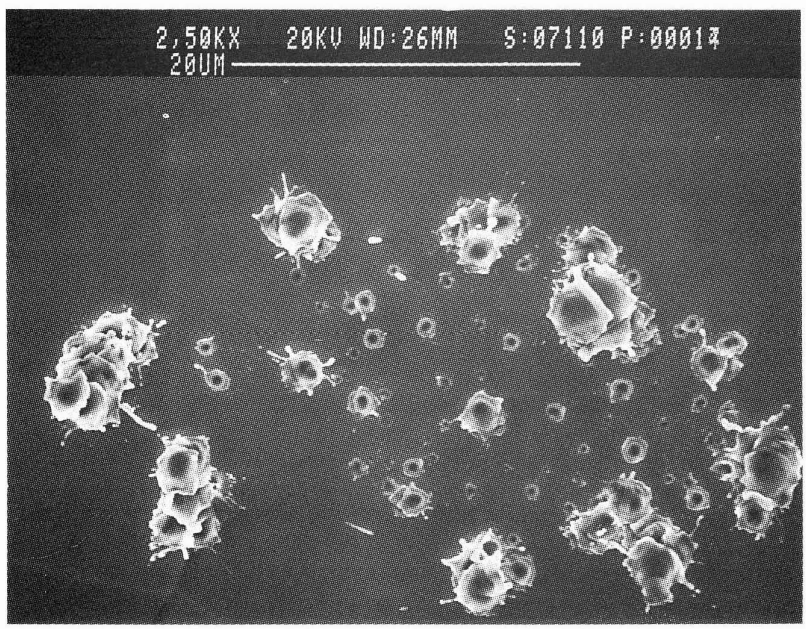

Figure 12b SEM micrograph of a dimple tested in the mushroom cavity showing clustered craters of molten niobium. Note the absence of ripples at this site.

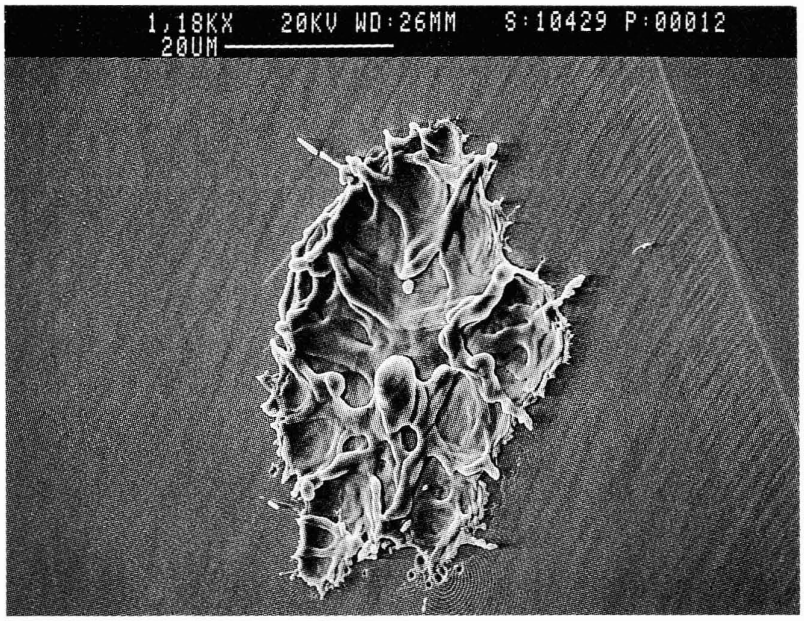

Figure 13a SEM micrograph of a 3 GHz S-band cavity showing overlapped craters of molten niobium. Ripples can be seen at the bottom of this micrograph.

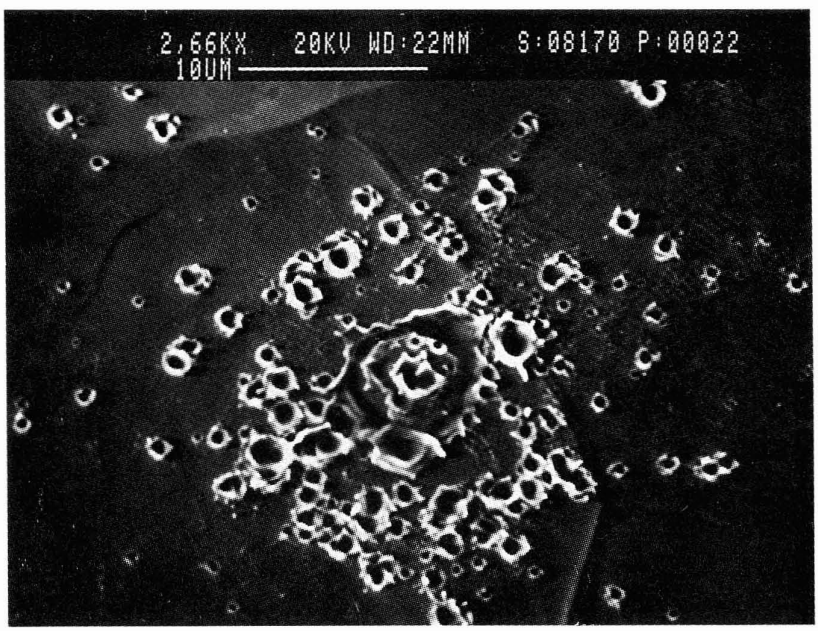

Figure 13b SEM micrograph of a 3 GHz S-band cavity showing nested craters of molten niobium.

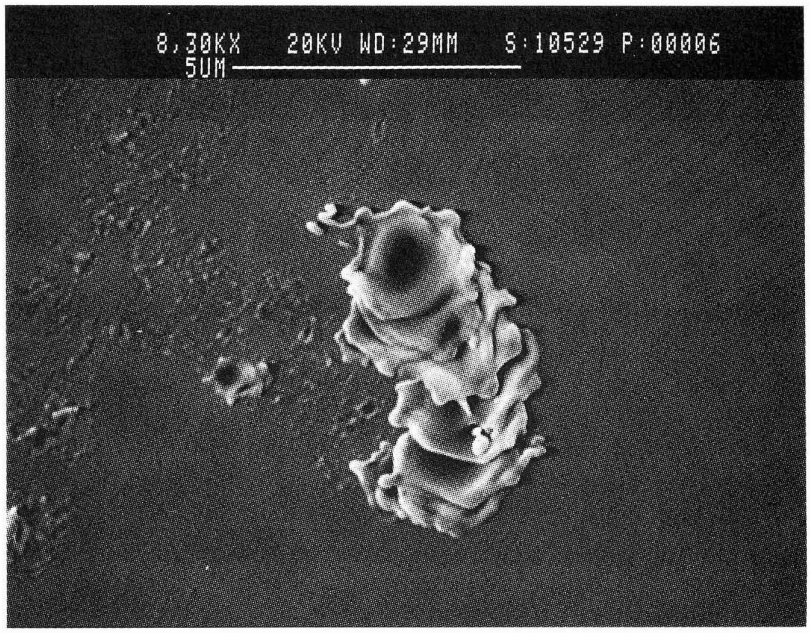

Figure 13c SEM micrograph of a 3 GHz S-band cavity showing a path of overlapped craters of molten niobium.

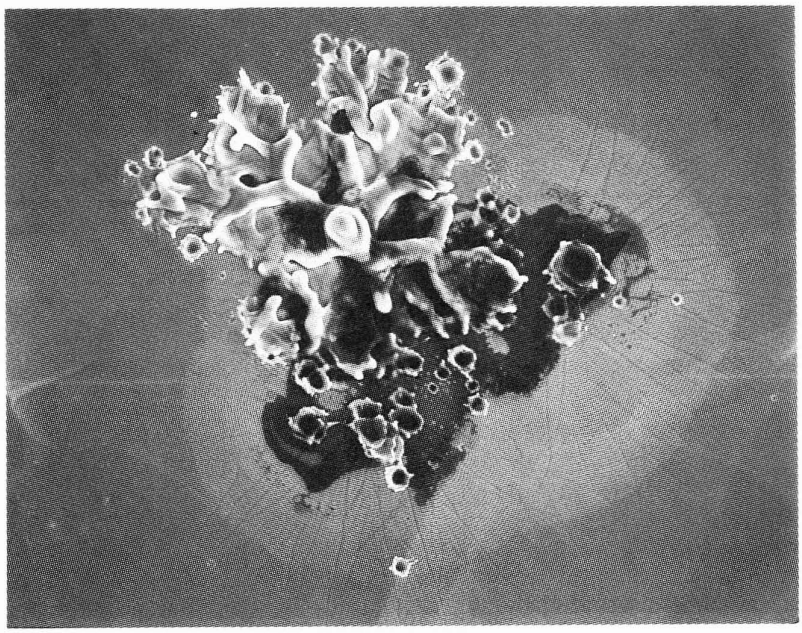

Figure 14a SEM micrograph of a dimple tested in the mushroom cavity showing overlapped craters of molten niobium. This micrograph was taken at near normal incidence.

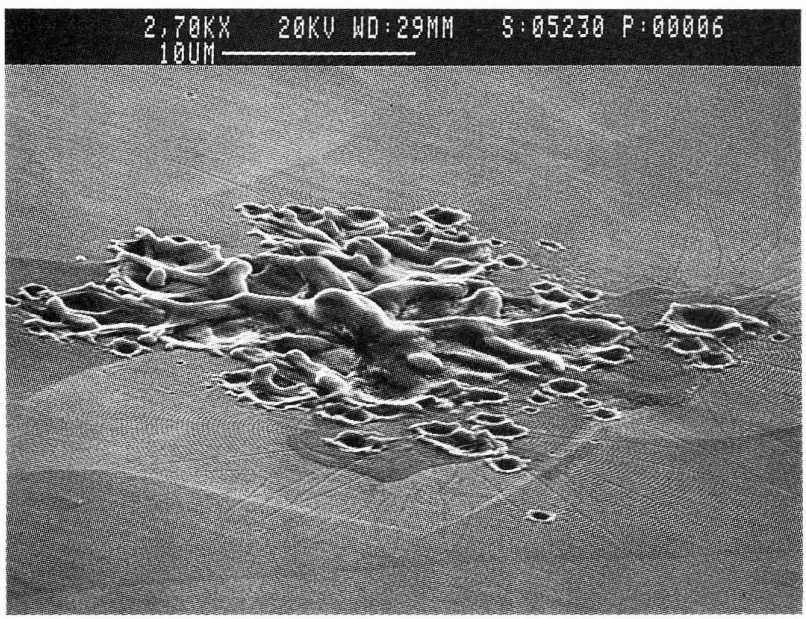

Figure 14b SEM micrograph of the craters shown in Figure 14a, but with the end-plate tilted ~40° from the normal.

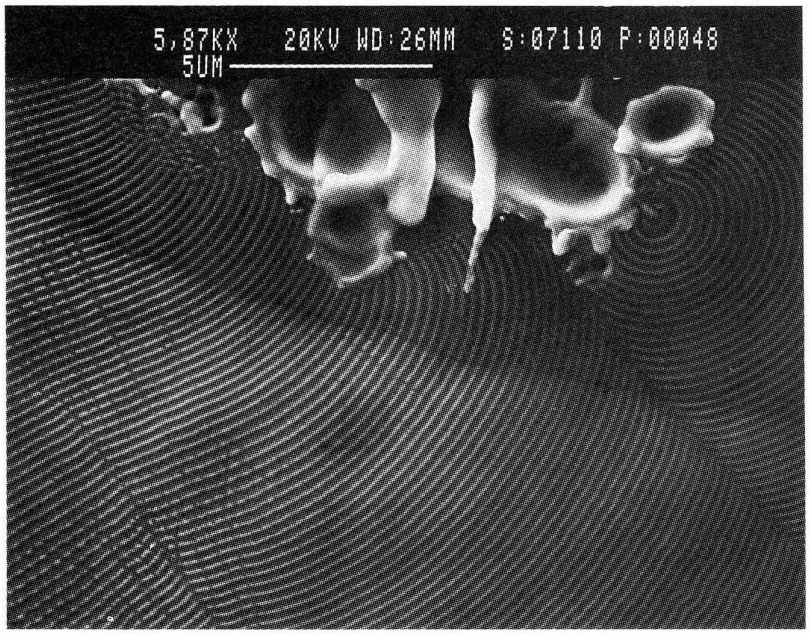

Figure 15 Higher magnification micrograph of the ripples shown in Figure 12a. Note the periodicity of the ripples and the matching at the discontinuity extending to the lower right-hand corner of the micrograph.

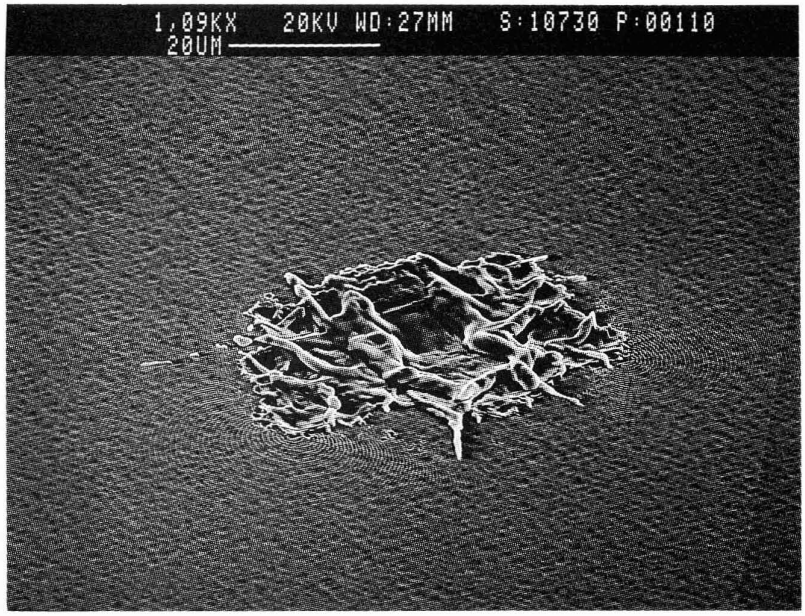

Figure 16a Low magnification SEM micrograph of a 3 GHz S-band cavity showing two ripple patterns emanating from overlapped craters of molten niobium.

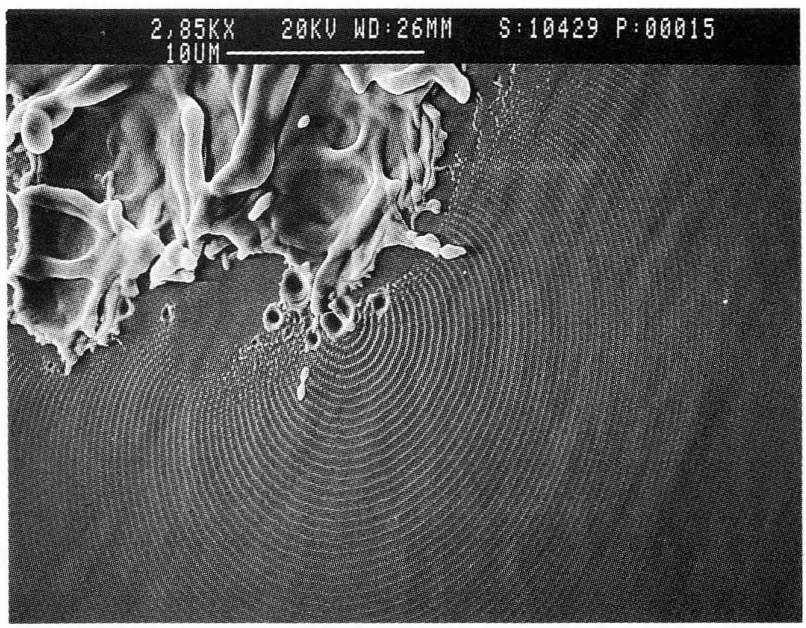

Figure 16b Higher magnification SEM micrograph of Figure 13a.

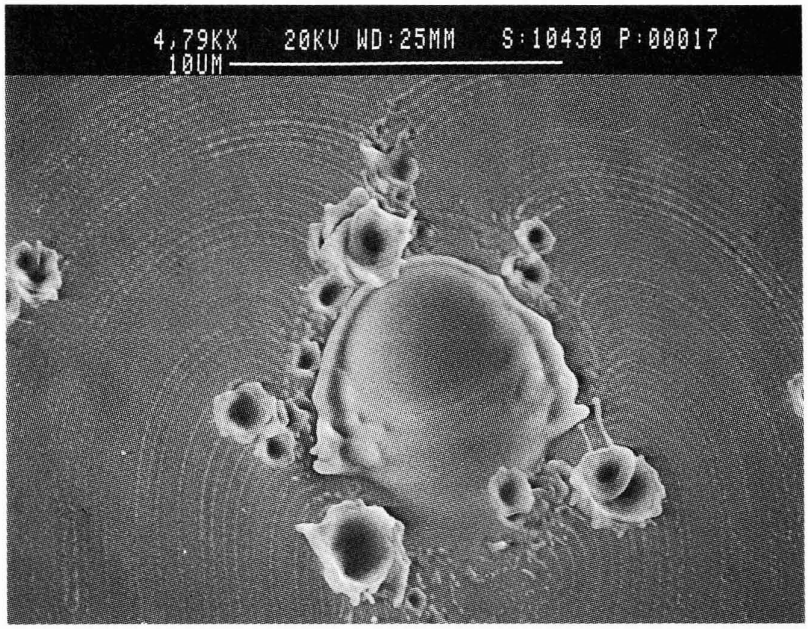

Figure 17 SEM micrograph of a 3 GHz S-band cavity showing a pattern of discontinuous ripples emanating from clustered craters of molten niobium.

Figure 18a SEM micrograph of a dimple tested in the mushroom cavity showing spheres of stainless steel close to a molten niobium crater. A starburst centered on the crater is just visible.

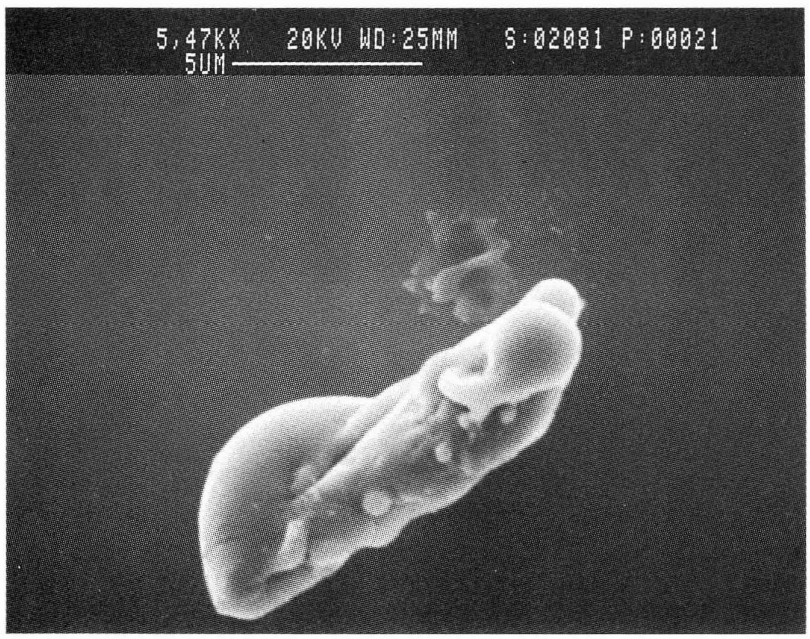

Figure 18b SEM micrograph of a dimple tested in the mushroom cavity showing another stainless steel particle. The ends of this particle appear to have melted. Note the faint crater just above the particle.

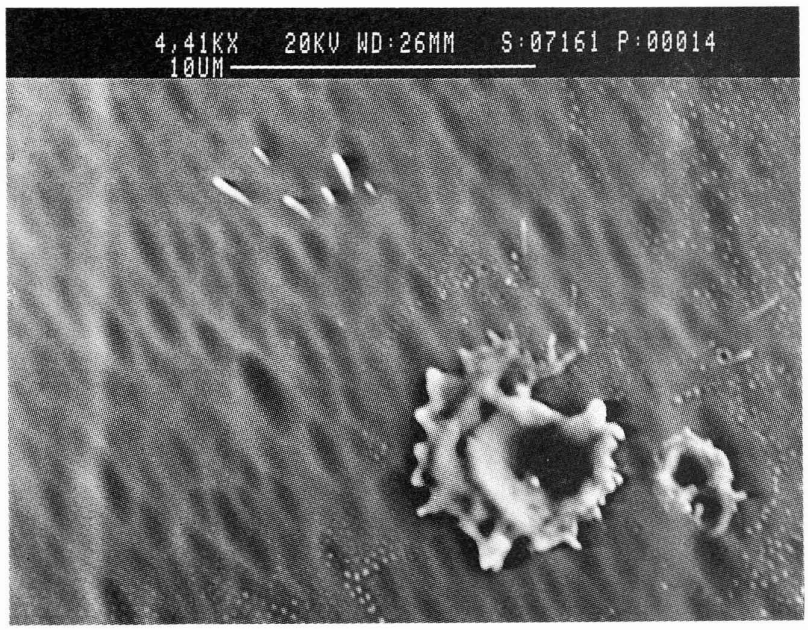

Figure 19a SEM micrograph of a 3 GHz S-band cavity. The six streaked features in the upper third of the micrograph gave a strong iron signal in EDS. The edges of the crater also gave a strong iron signal.

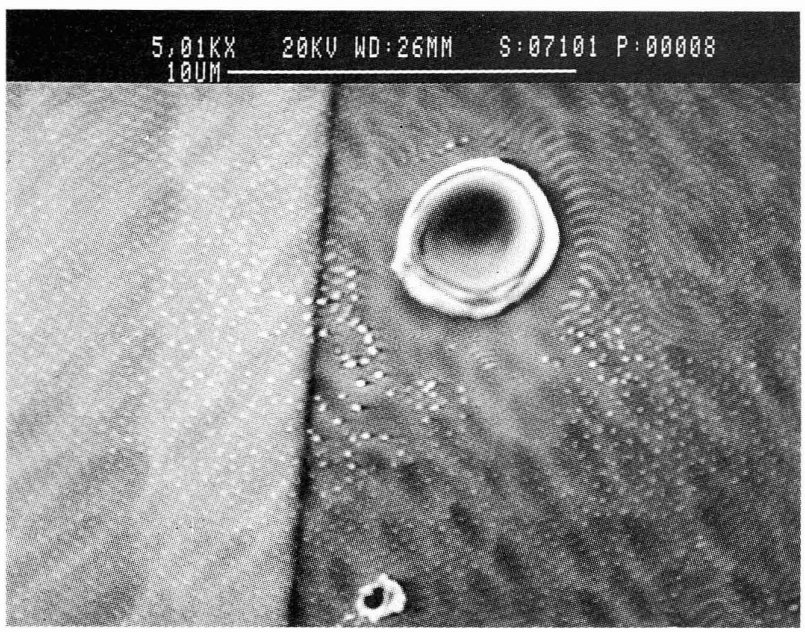

Figure 19b SEM micrograph of a 3 GHz S-band cavity. No particles are visible, but the edges of the crater gave strong iron and chromium signals.

Figure 20a SEM micrograph of a 3 GHz S-band cavity showing the splashed remains of an indium particle.

Figure 20b SEM micrograph of a 3 GHz S-band cavity showing the splashed remains of an indium particle. A feature similar to this was found at the center of the starburst shown in Figure 9a.

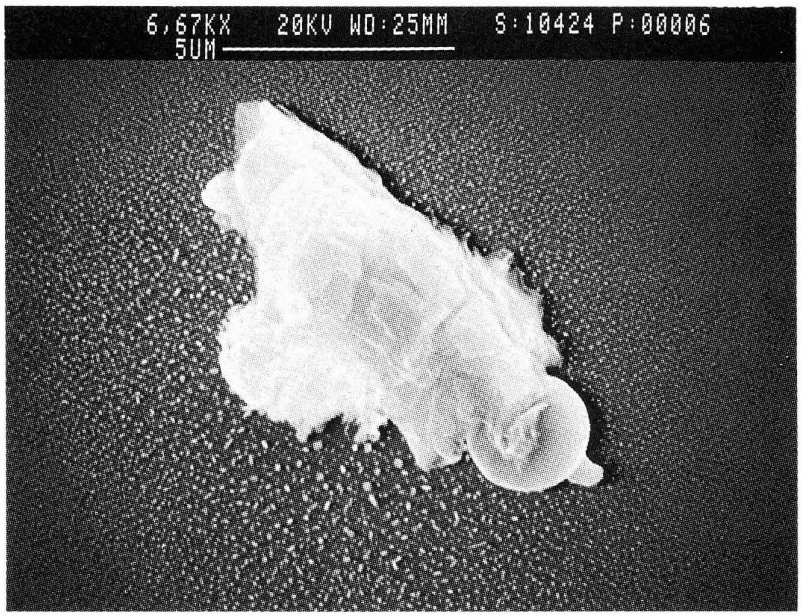

Figure 21 SEM micrograph of a 3 GHz S-band cavity showing an indium particle. Note that the lower right end has melted. The dust surrounding this particle is too fine to analyze using EDS.

Figure 22a SEM micrograph of a dimple tested in the mushroom cavity showing particles containing copper, iron and indium.

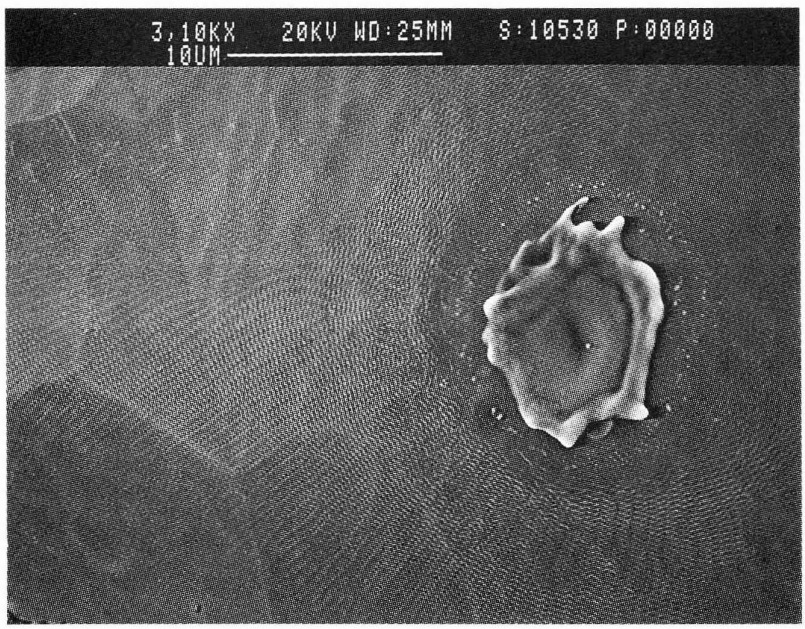

Figure 22b SEM micrograph of a 3 GHz S-band cavity showing a copper particle at the center of a crater.

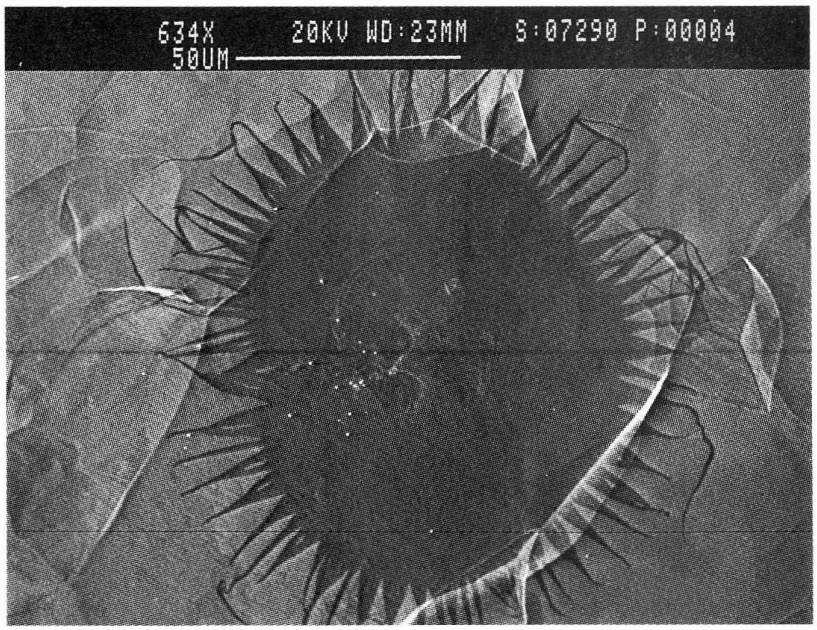

Figure 23 SEM micrograph of a dimple tested in the mushroom cavity showing particles containing titanium.

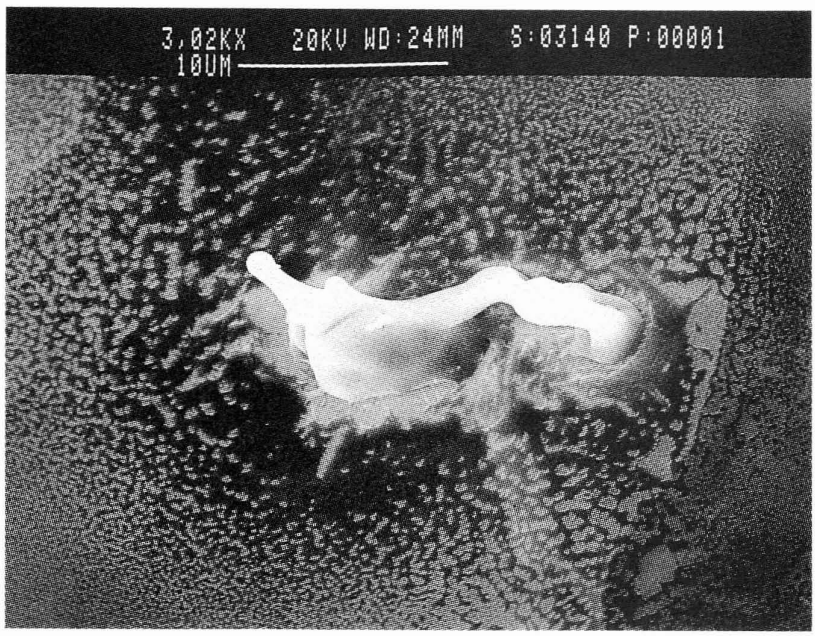

Figure 24 SEM micrograph of a dimple tested in the mushroom cavity showing a teflon particle. Note the melted ends. The peak surface electric field at this particle was ~40 MV/m.

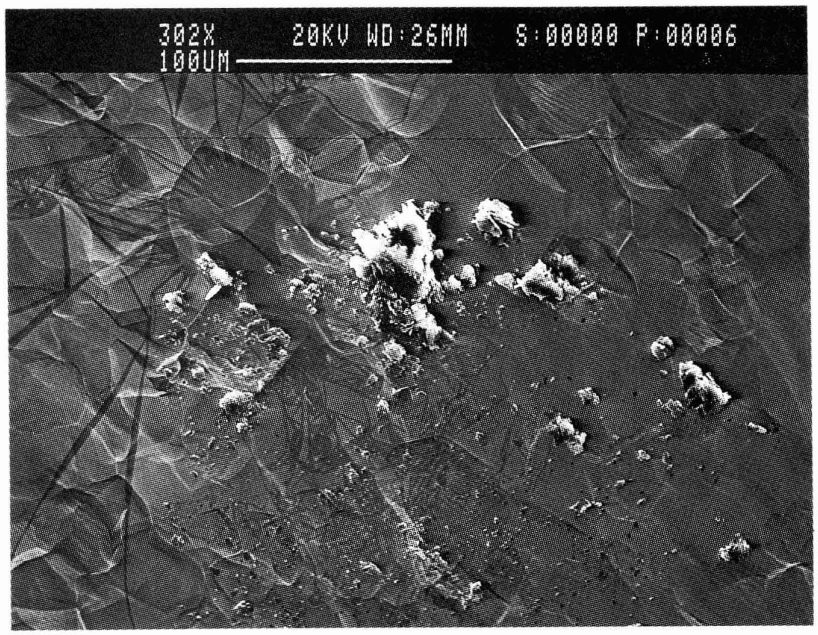

Figure 25a SEM micrograph of a dimple tested in the mushroom cavity after placing carbon flakes on the dimple. This micrograph was taken after the peak field had been raised to 25 MV/m. Several of the carbon flakes are still visible. A starburst and some tracking are also visible.

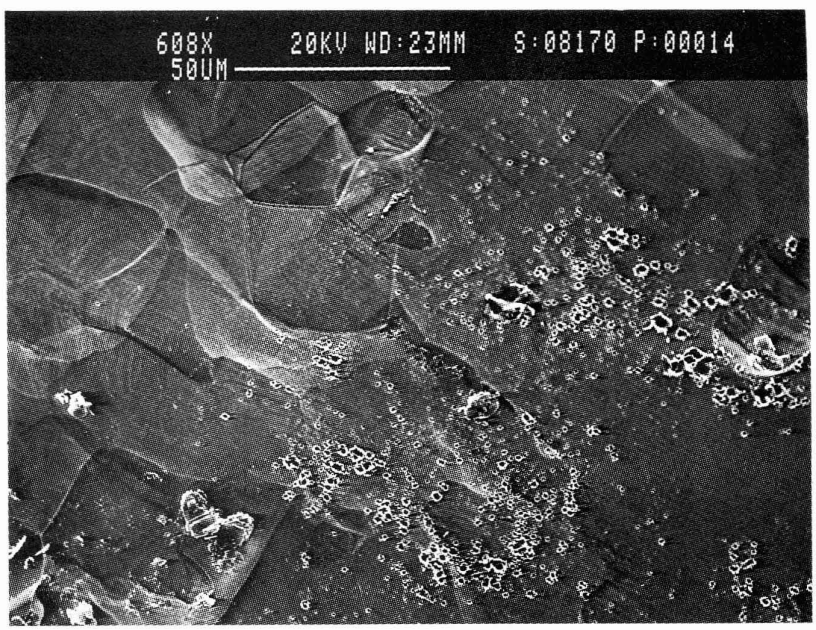

Figure 25b SEM micrograph of the same area shown in Figure 25a, but after the peak field had been raised to 60 MV/m. Only one or two of the carbon flakes are still visible. Extensive crater fields are now visible.

DISTRIBUTION OF SITES IN AN ACCELERATING CAVITY

Temperature and x-ray maps have indicated that electron emission activity occurs at the irises of accelerating cavities. We were able to verify this by examining the half-cells of the cut S-band cavities. Figure 26 shows the distribution of starbursts found on the half-cells. It is clear that the starbursts were found in the high electric field region.

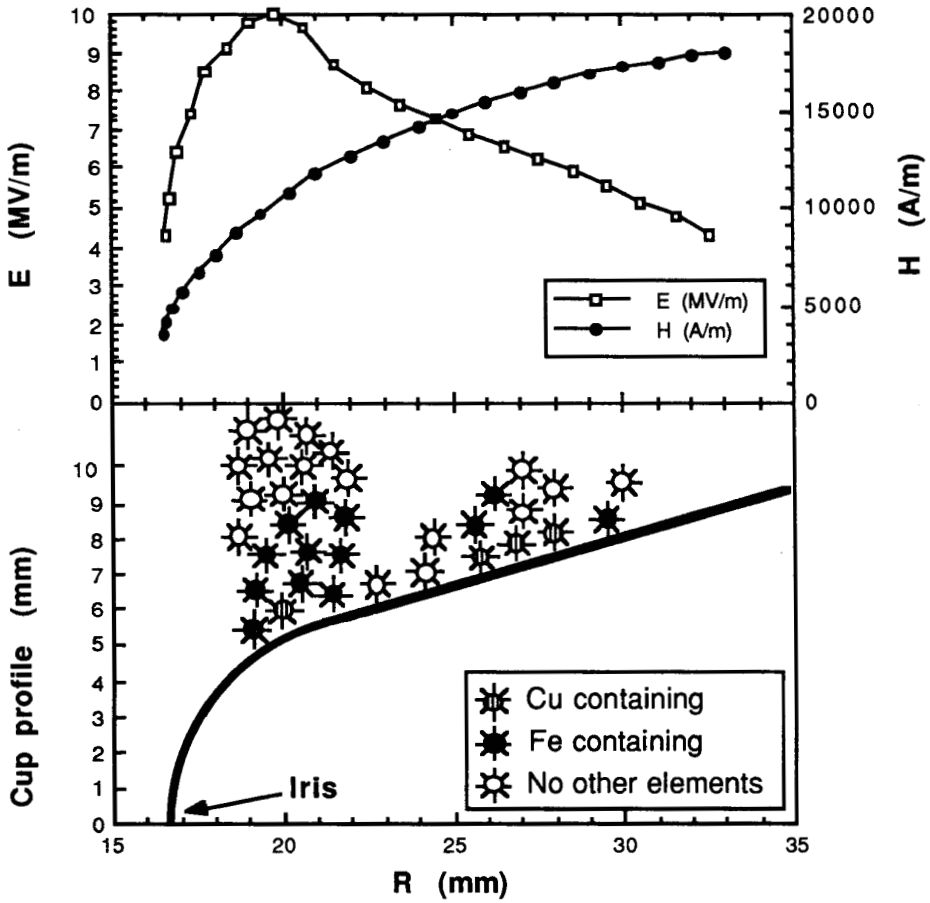

Figure 26 Location of starbursts in three 3 GHz, S-band cavities. No differentiation as to whether a starburst was found on the top or bottom half has been made here. The indium containing starbursts are not included in this figure.

Care was taken to document whether starbursts were found on the upper or lower half-cell of an S-band cavity. (This nomenclature refers to the orientation during testing.) The results are summarized in the table below. It is clear that more than twice as many starbursts were found on the lower half-cell than on the upper half-cell. This is interesting in view of the fact that these cavities were evacuated from the bottom and the adjustable input RF coupler also was below the cavity. In the one test which suffered from indium contamination, it was equally likely to find starbursts containing indium on either the upper or lower half-cell.

TABLE I

Occurrence of starbursts on S-band cavity half-cells

Test #	# of Starbursts	# on Upper Half-cell	# on Lower Half-cell
1	18	4	14
1 (indium)	19	10	9
2	2	0	2
3	15	1	14
Totals	54	15	39

THE CREATION OF MOLTEN NIOBIUM CRATERS

Our observations show that a small region of a superconducting niobium cavity surface can melt and form craters through a process that includes field emission. Current emitted from an emitter must flow through the niobium cavity wall in order to be emitted through the emitter. If the cavity wall is resistive, this flow of current will cause heating. The current required to melt an area of niobium cavity surface on the order of $1\mu m^2$ now needs to be calculated.

For the purposes of this discussion, it will be assumed that the current flows through a niobium cylinder of length ℓ which intersects the RF surface in a circle of radius r. The radius of this cylinder is determined by the emitter, i.e. the exposed end of this cylinder is covered by something which enhances the surface electric field (see Figure 27). Also, it will be assumed that this cylinder is thermally isolated from the rest of the cavity wall. This may be effected by a low thermal conductivity boundary. If it is possible for this cylinder to heat so rapidly that heat cannot diffuse away, a temporal thermal isolation will exist. The known fact that a restricted portion of the niobium surface can melt implies that there must be thermal isolation on some time and length scale.

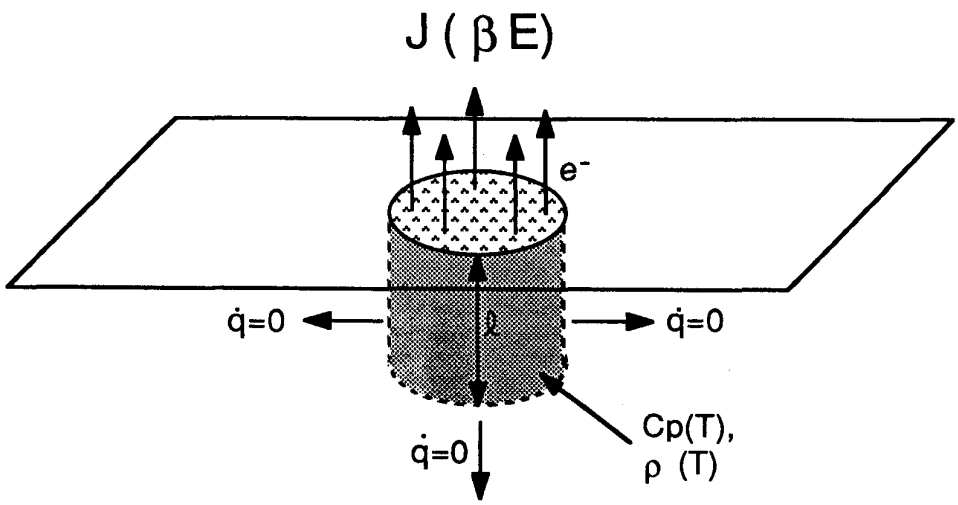

Figure 27 Schematic of the volume in the niobium cavity wall through which the emitted current must flow.

Heating of the Emission Site

The end of this hypothetical niobium cylinder is exposed to the applied H field as well as to the E field. The power dissipated by the applied H field in an area of radius r is given by:

$$P_{diss} = \frac{1}{2} R_s \int H^2 \, dA \approx \frac{1}{2} R_s H^2 \pi r^2 \tag{1}$$

where R_S is the surface resistivity. It turns out that this is orders of magnitude less than that due to the resistive heating caused by the emitted current. For this reason it will not be considered further.

To calculate the heating caused by the passage of the emission current, we begin with the "Fowler-Nordheim" equation as given by [8]:

$$j = \frac{e^3}{8\pi h \phi t^2(y)} F^2 \exp\left(-\frac{8\pi(2m\phi^3)^{1/2}}{3 e h F} v(y)\right) = 38.5 \frac{F^2}{t^2(y)} \exp\left(-54640 \frac{v(y)}{F}\right) A/cm^2 \tag{2}$$

$$y = \left(e^3 F/\phi^2\right)^{1/2} = .00948 F^{1/2} \tag{3}$$

where F is the applied electric field in MV/m and a value of 4 eV has been used for ϕ. (It is interesting to note that this equation does not appear in this complete form in any publication by Fowler or Nordheim.) Standard practice is to substitute an enhanced field, βE, for F in the "Fowler-Nordheim" equation but not in the equation for y. When this latter substitution is not made, the functions v(y) and t(y) are close to unity and are customarily omitted. We prefer to substitute βE for *all* occurrences of F. Doing this necessitates the inclusion of v(y) and t(y) in emission current calculations and results in emitted currents approximately two orders of magnitude greater for the same βE values. The functions v(y) and t(y) as given in [17] are the most useful. The currents calculated in this manner are plotted in Figure 28.

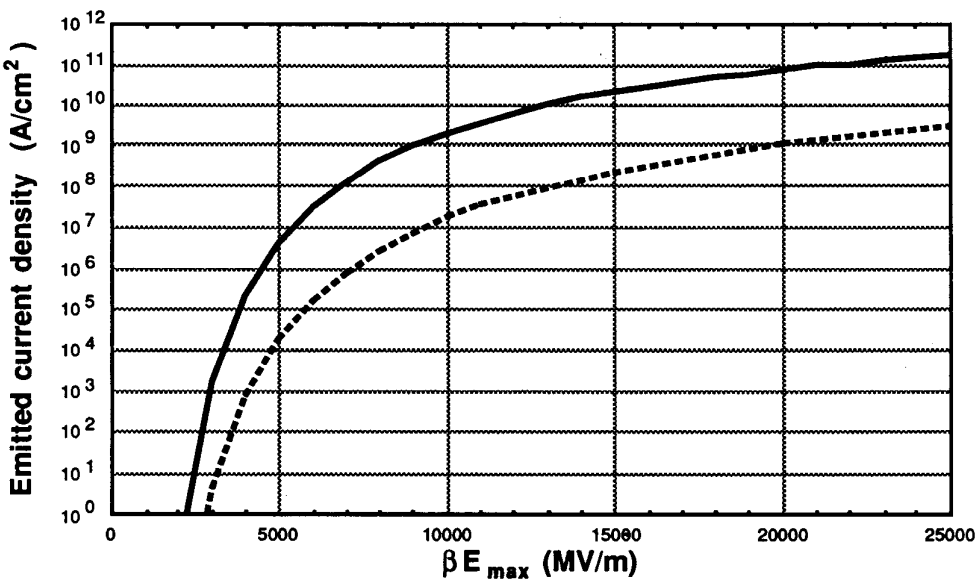

Figure 28 Comparison of calculated field emission currents using equations 2 and 3 with and without v(y) and t(y). βE was substituted for F in equation 3 when v(y) and t(y) were included. The calculations which included v(y) and t(y) are drawn with a solid line.

At this point, a few comments concerning the choice of the Fowler-Nordheim formalism and the use of β are in order. The "Fowler-Nordheim" equation predicts the observed functional dependence of emitted current on field, provided that an enhancement factor is used. For the purposes of this discussion, this is a sufficient reason for its choice. There has been much controversy as to the unphysically large β values required to bring calculation and experiment into agreement. In general, the origin of β for any specific emitter is unknown and it may vary from emitter to emitter. Since the use of β is empirical, the fact that a reduction factor for φ may be included in it must not be ignored. Therefore, until more is known about the nature of actual RF emitters, any explanation of the magnitude or origin of β is presumptuous.

The power dissipated in a cylinder of length ℓ and radius r by the flow of current along its axis is given by:

$$P_{diss} = I^2R = j^2(\pi r^2)^2 \frac{\rho \ell}{\pi r^2} = j^2 \pi r^2 \rho \ell \tag{4}$$

where ρ is the DC resistivity of the cylinder and j is the current density. The emitted current density is a function of the surface E field and, therefore, a function of time, while the resistivity is a function of the temperature of the cylinder. The temperature increase of the cylinder is:

$$\Delta T = \frac{\left(j^2 \pi r^2 \rho \ell\right)}{C_p \pi r^2 \ell} \Delta t = \frac{j^2(t)\,\rho(T)}{C_p(T)} \Delta t \tag{5}$$

where C_p is the specific heat of the cylinder and t is time. It should be noted that neither the length of the cylinder, nor its radius, enters into this equation. The temperature dependence of C_p [18] and ρ [19, 20] (300 RRR) for niobium are given in Figures 29 and 30. Once the melting point of niobium (2740K [21]) is reached, the heat of fusion, ΔH_m, must be supplied before the cylinder of niobium may actually melt. The heat of fusion of niobium is ~2400 J/cm^3 (2.4 nJ/μm^3) [21]. Using this and the data in Figure 29, one finds that the energy required to melt niobium originally at 10K is ~10 nJ/μm^3; the energy needed to melt niobium at 2740K is only ~2.4 nJ/μm^3. For craters of the size observed in the SEM, the energy required to form them is many orders of magnitude less than the stored energy in a cavity. This means that the formation of a molten crater will not cause the fields in a cavity to collapse.

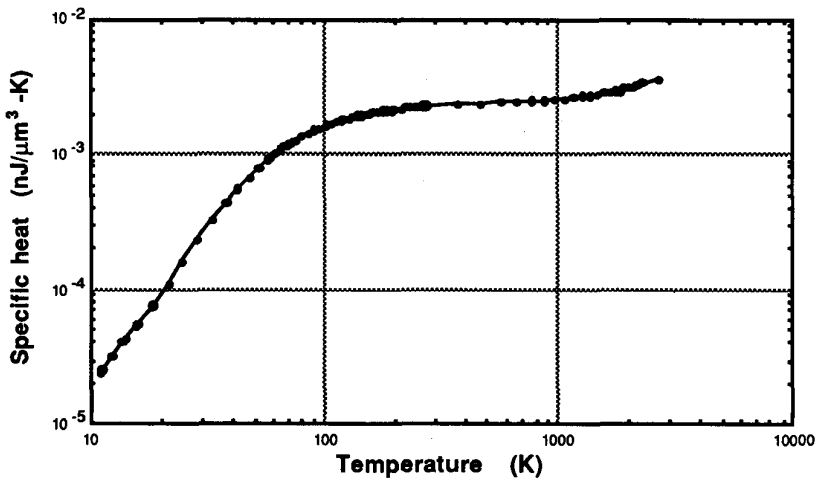

Figure 29 The measured specific heat of niobium.

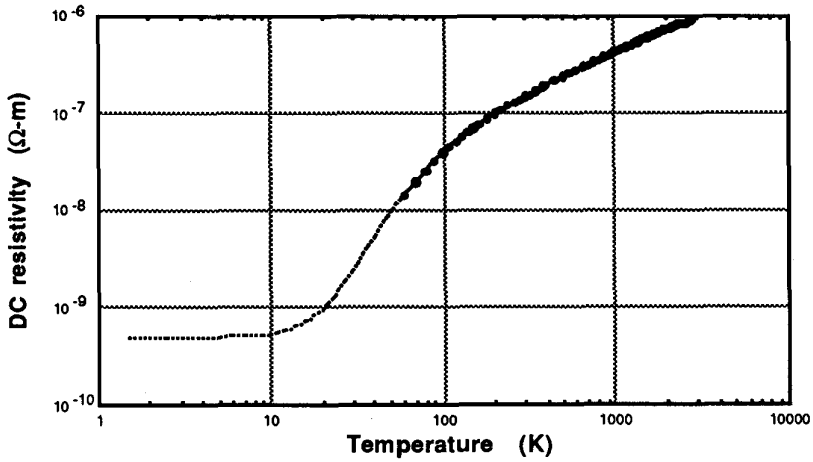

Figure 30 The measured and calculated values for the resistivity of niobium as a function of temperature. The values calculated for 300 RRR niobium are drawn with a dotted line and are based on the equation of [19].

Niobium Vapor Pressure and Gas Density

The DC literature contains several references to the density of a plasma which enables a spark to bridge the vacuum gap. For comparison with that literature, the vapor pressure of niobium, and an estimate of the densityof a niobium gas cloud over an emission site will be calculated here. The vapor pressure of niobium is given by [22]:

$$\log_{10} P_v = \frac{-37650}{T} + .715 \log_{10} T - 1.66 \times 10^{-4} T + 8.72 \qquad (6)$$

where P_v is in torr and T is temperature in kelvin. The rate of niobium evaporation from a surface may be calculated assuming a Knudsen cell was used to measure the vapor pressure [22]:

$$\frac{m}{tA} = P_v \left(\frac{M}{2\pi RT}\right)^{1/2} = 5.63 \times 10^{-9} \frac{P_v}{T^{1/2}} \frac{g}{sec \cdot \mu m^2} \qquad (7)$$

where m is the evaporated mass, M is the molecular weight of the evaporating species, A is the evaporating area, t is time and P_v is the vapor pressure in torr. The thermal velocity of the vaporized niobium atoms is:

$$v_T = \left(\frac{3RT}{M}\right)^{1/2} = .0164\, T^{1/2}\ \mu m/nsec \qquad (8)$$

The units μm/nsec are convenient to use because of the length and time scales associated with crater formation. The RMS velocity of a singly ionized niobium atom in an electric field over one half RF period is given by:

$$v_i = 2^{-1/2} \frac{eE_{peak}}{M/N_A} \frac{1}{2f} = .367 \frac{E_{peak}}{f}\ \mu m/nsec \qquad (9)$$

where E is in MV/m and f is the RF frequency in GHz. (The average velocity over a whole RF period is, of course, zero.) If we assume that the vaporized niobium atoms move at the thermal velocity and expand axially in a cylinder above the emission region, the density of atoms in this cylinder can be shown to be:

$$\frac{n}{V} = P_v \left(\frac{M}{2\pi RT}\right)^{1/2} \left(\frac{M}{3RT}\right)^{1/2} \frac{N_A}{M} = \frac{P_v}{T} \frac{1}{(6\pi)^{1/2} k_B} = 2.22 \times 10^{18} \frac{P_v}{T} \text{ cm}^{-3} \quad (10)$$

where N_A is Avogadro's number and k_B is the Boltzman constant. This equation yields the plasma density when the niobium atoms are singly ionized. For comparison, the ideal gas law gives:

$$\frac{n}{V} = \frac{P_v}{T} \frac{1}{k_B} = 9.64 \times 10^{18} \frac{P_v}{T} \text{ cm}^{-3} \quad (11)$$

To provide points of reference, the values of all of these quantities at the melting and normal boiling points are given in the following table. These will be compared with values from the DC literature in a later section.

TABLE II

Calculated values of vapor pressure, ion velocity and plasma density

	2740 K	5017 K
P_v (torr)	9.6×10^{-4}	760
v_T (μm/nsec)	.86	1.2
v_i (μm/nsec) @ 50 MV/m	6.1 (@ 3 GHz)	3.1 (@ 6 GHz)
n/V (cm^{-3})	7.8×10^{11}	3.4×10^{17}

Boiling at the Emission Site

When the niobium cylinder melts, it is technically above the boiling point. The boiling point of a substance is defined as the temperature at which its vapor pressure equals the ambient. At 2740K, the vapor pressure of niobium is .96 mtorr. The ambient pressure in a cavity in superfluid helium is less than 10^{-9} mtorr. (Using equation 6, the boiling point at this pressure should be ~1660K.) Therefore, it should be expected that niobium vapor bubbles will form very quickly in the molten surface. As these bubbles grow and coalesce, they will eventually burst. The point at which they burst will be determined by size of the bubble and the surface tension of the liquid niobium.

Time Dependence of Emitter Heating

Figure 31 shows the time dependence of the temperature of the niobium cylinder under an emitter for three different values of βE_{max}. Each RF period was divided into twenty steps in these calculations, and the initial temperature of the cylinder was originally 10K, or at least not superconducting. This latter point can be justified on the basis of the critical current density of superconducting niobium being exceeded or by heating due to the Nottingham effect. The thermal conductivity at the cylinder/bulk interface was assumed to be zero.

When the surface becomes sufficiently hot, electrons will be thermionically emitted as well. The passage of the thermionic current through the niobium cylinder will cause additional heating. This effect is strongest when the βE_{max} of the emitter is low. Calculations have shown that this decreases the time required to reach the melting point by about a factor of two. Because the inclusion of thermionic emission effects is complex and still under development, it will not be discussed further in this paper.

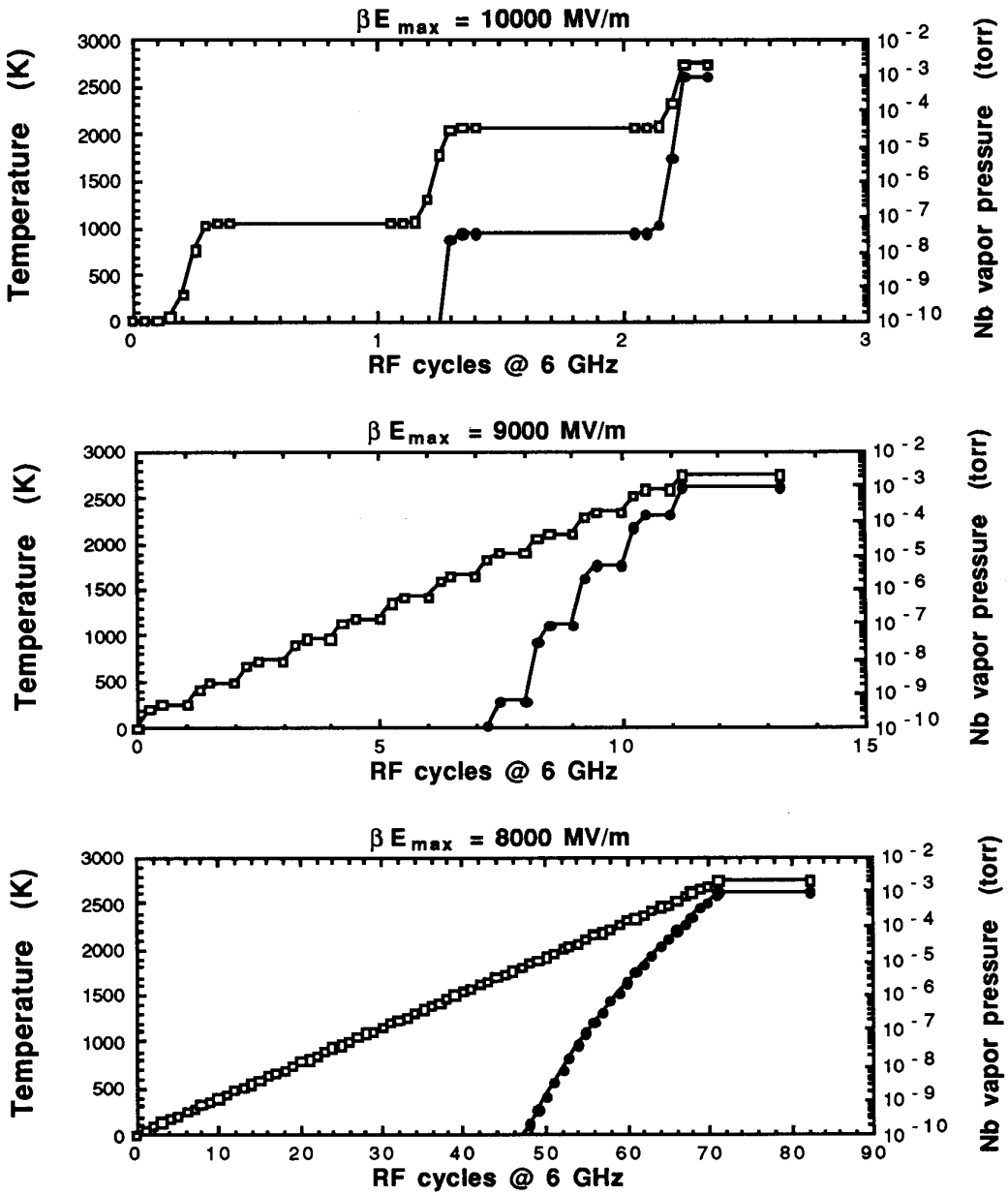

Figure 31 The heating of a niobium cylinder as a function of RF period for three different values of βE_{max}. The calculated niobium vapor pressure corresponding to the emitter temperature at a given point in the RF cycle is drawn with filled circles.

The times required to reach the melting point as a function of βE_{max} are summarized in Figure 32. It can be seen that for βE_{max} values greater than 8000 MV/m, it takes only 10 nsec or less for the niobium cylinder to reach 2740K. Once at the melting point, ten or fewer RF cycles are required to supply the heat necessary to melt the cylinder. This time scale is clearly too short for the thermal conductivity of the cavity wall to have an effect. Assuming that processing, i.e. destruction, of the emitter occurs soon after melting, emitters with these very high βE_{max} values will process quickly and easily.

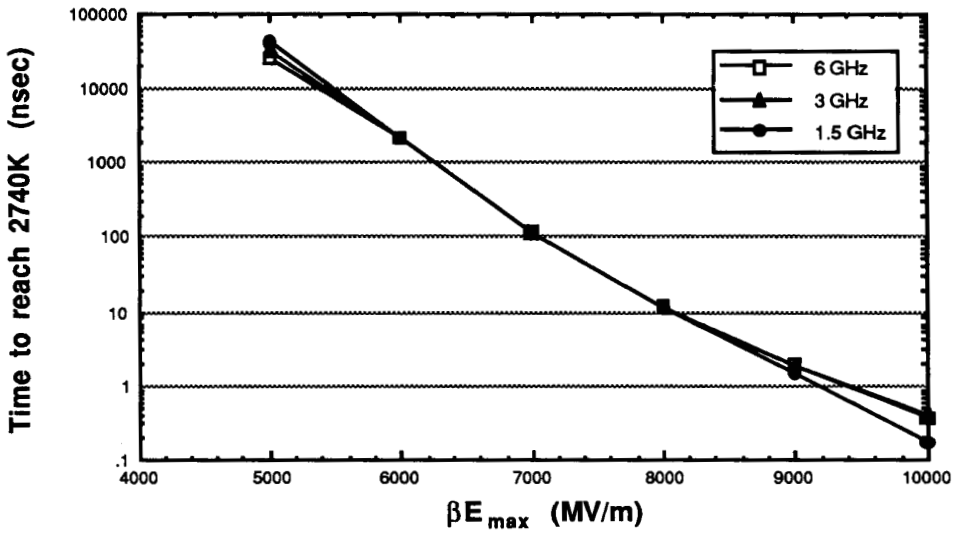

Figure 32 The calculated times for a niobium cylinder to reach 2740K as a function of βE_{max}. Only the heating due to the field emission current has been calculated, i.e. effects due to thermionic emission were not included.

Emitters with βE_{max} values less than 8000 MV/m may remain in the near-molten state for a considerable length of time (Figure 33). If βE_{max} is lowered to 5000 - 6000 MV/m, the time required to reach the melting point is so long that the thermal conductivity of the cavity wall may cause the diffusion of some of the heat away from the emission site. These emitters will be more difficult to process. Emitters with βE_{max} values less than 3000 MV/m have an emitted current density of less than 10^3 A/cm^2, which should be less than the critical current density of niobium. These emitters are expected to be stable, and because of the low currents involved may not even cause any heating.

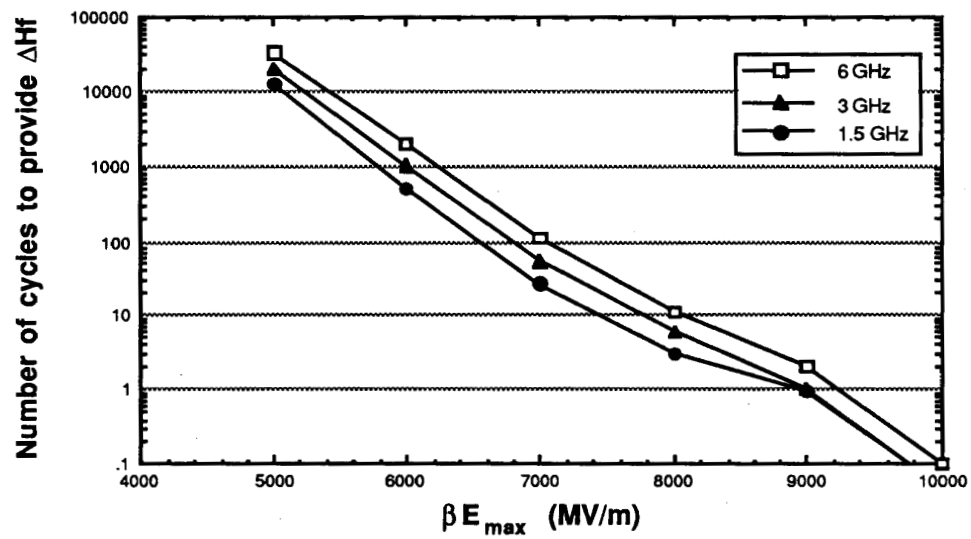

Figure 33 The calculated number of RF cycles required to supply the heat of fusion, ΔH_f, to an emission site at 2740K as a function of βE_{max}.

Figure 34 is an updated version of Figure 21a from the review on field emission given at the 4th Workshop on RF Superconductivity [23]. (The βE_{max} values are different, reflecting the present implementation of βE_{max} in the "Fowler-Nordheim" equation.) The emitters in this graph were compiled as part of field emission studies in 1.5 GHz cavities. All but four of the emitters in this graph were stable emitters. The data in this graph roughly reflect the surmises of the discussion above. It should be remembered that emission, the location of emitters, and the processing of emitters are all statistical in nature, so that the persistence of some emitters with high βE_{max} values is not unexpected.

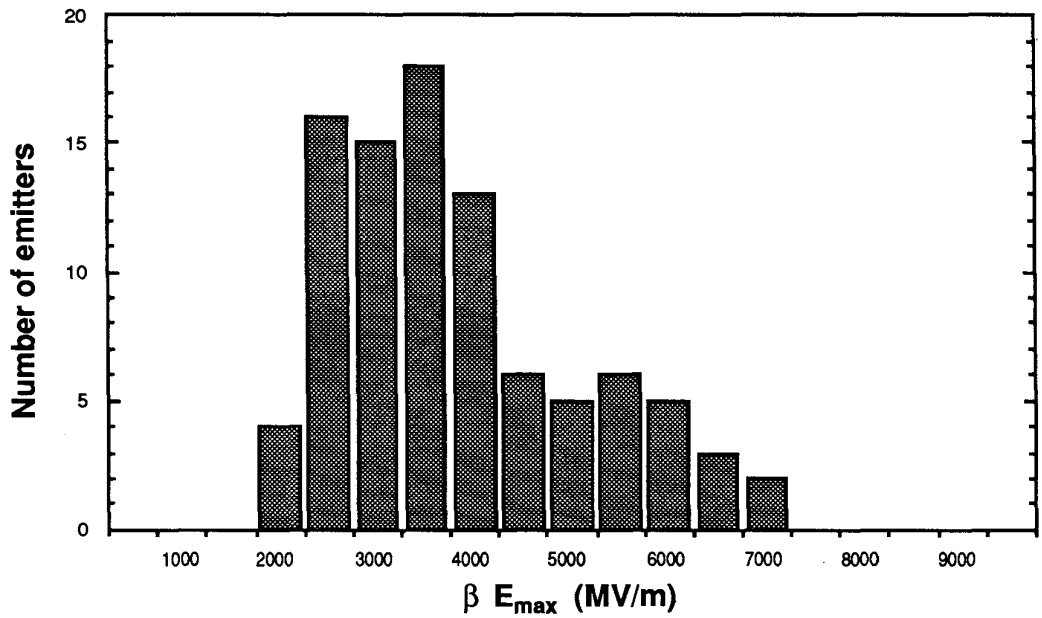

Figure 34 The frequency of emitters found in 1.5 GHz cavities by thermometry.

EMITTER PROCESSING TECHNIQUES

An emitter can be processed either by physical or chemical modification, or by destroying it. High temperature heat treatments of cavities prior to testing have been successful in reducing field emission. Heat treatments may enable the dissolution of emitting inclusions and/or absorption of any surface microprojections.

During cavity testing two techniques may be used to process emitters: helium processing and high peak power pulsed processing. Again, assuming that emitter processing occurs soon after the underlying niobium melts, the key to *in situ* processing is to increase βE_{max} to the point where the emitted current density is high enough to cause melting. It is unknown whether helium processing effects a reduction of β, or if it increases β so that the emitter is processable at the applied E field. (We have not yet examined helium processed surfaces with the SEM.) High peak power pulsed processing increases the applied E field for only a very brief time, ~5 μsec, but the micrographs indicate that this is sufficient to cause the destruction of emitters. On this basis, the benefits derived by pulsed processing would be expected to survive exposing the cavity to dry, filtered air.

COMPARISON WITH DC STUDIES AND STUDIES ON COPPER RF CAVITIES

There is an extensive body of work in the literature regarding DC field emission and vacuum electrical breakdown. The sequence of events in vacuum breakdown, as developed in the DC literature, are: 1) field emission results in heating of the emission site; 2) explosive electron emission occurs creating a plasma; 3) an arc forms, yielding a visible glow or spark. Repetition of this process gradually results in an increase of the field at which breakdown occurs, i.e. electrode conditioning. Micrographs of the surfaces of electrodes showing craters created during breakdown appear in several papers [e.g. 24–28]. Post-mortem studies of copper RF cavities which suffered from RF breakdown revealed multiply cratered surfaces [29,30]. The starbursts and ripple patterns shown in the present paper have not been reported in the literature.

The values of several parameters important to the processing of emitters have been calculated/estimated/measured: breakdown times of nanoseconds to microseconds [26, 27]; emitted current densities of up to 10^9 A/cm^2 [26, 27]; plasma densities of 10^{20} cm^{-3} or greater [26, 27, 31]; cathode flare velocities of ~10^6 cm/sec (~10 μm/nsec) [26, 32]. Using similar emitted current densities, this study has calculated times to surface melting on the same order of magnitude as the DC breakdown times. The calculated thermal velocity of niobium atoms agrees with the measured cathode flare velocities. The only apparent discrepancy is that the niobium gas density calculated in this paper is orders of magnitude less than the plasma densities quoted in the DC literature. This may call into question the role that the plasma plays in emitter processing, or perhaps the motion imposed on the plasma by the electric field causes a compression of the vapor cloud, increasing its density. In addition, the model briefly described above indicates that the emission site melts and explodes before the plasma is created, whereas the non-negligible vapor pressure of the cavity material dictates that a vapor cloud will exist prior to melting. The fact that a molten emission site may boil appears to have been completely neglected in the literature.

CONJECTURES AS TO THE NATURE OF EMITTERS

Much remains to be learned about the sequence of events starting with localized field enhancement and ending with molten craters surrounded by starbursts. The extent to which an enhancement mechanism survives temperatures as high as 2740K is unknown. However, the present state of this investigation does allow us to make some reasonable conjectures as to the nature of some emitters.

The remains of contaminant particles have been found at the centers of many starbursts. These particles were resting on the niobium surface, and, in most cases, had been partially or fully melted, as evidenced by their spherodization. When indium was found in a starburst, no molten niobium craters were found. When higher melting point particulates, i.e. iron, stainless steel, copper, etc., were found, only a few niobium craters were found nearby. This evidence suggests that metallic particles on the RF surface enhance the local electric field, are heated by the emitted current and eventually melt. If the particulate emitter has a low melting point, it is processed before the current density is high enough to cause melting of the niobium surface. On the other hand, no foreign elements were detected in the massive, multiply cratered regions. If particulates were the original emitters at these sites, they must have been completely vaporized by processing.

The fact that some emission sites sustain repeated cratering indicates that the operative enhancement mechanism at these sites is either thermodynamically stable enough to withstand several melting cycles, or that it regenerates itself after melting. Any adsorbed surface contamination would be expected to vaporize, dissolve or react with the niobium surface the first time the site reached the melting point. Unless a layer of contamination reforms, it is unlikely that this could persistently enhance the field or cause a reduction in the work function. It has been suggested that a micropoint formed at the edge of a crater may serve as the next emission site [27, 31]. However, the forces of surface tension should cause it to smooth out as soon as it melted. Interstitial inclusions may enhance the local electric field, but of the possible interstitial compounds, i.e. hydrides, carbides, nitrides or oxides, only NbC is stable above 2740K (it decomposes congruently at ~3900K) [33]. By coincidence, this study and others used carbon as an introduced emitter.

SUMMARY

One goal of this research project is to identify actual RF emitters. Important strides have been made in visualizing the effects of processing, but we have only seen emission sites after they have been processed. Clear identification of an active emitter remains to be accomplished. Careful studies of emission activity using an S-band cavity with thermometry may yield the desired results.

Particulate contamination has been clearly shown to be associated with emission. The contamination problem persists even when cavity assembly is performed in clean rooms. The development of appropriate procedures and the diligence of personnel in adhering to them is crucial to maintaining a particulate-free surface throughout cavity assembly.

Future work will, hopefully, be more succesful in identifying emitters. The possibility that NbC emitters are responsible for the emission limiting present cavities must be explored further. High temperature heat treatments will help to dissolve these inclusions, but times and temperatures will need to be adjusted for complete dissolution. Further studies should implant oxides and nitrides and examine the resulting emission sites to see if the same multiply cratered surface is created.

The differences and similarities with DC field emission need to be better understood. The roles of plasmas and site boiling need to be examined more closely. Of great value to the RF community would be future FESM studies which examine the emission regime relevant to RF emission and processing, i.e. emitted current densities greater than ~10^6 A/cm^2.

The present study has revealed a wealth of new information about the nature of field emission sites and the results of processing in RF superconducting niobium cavities. None of the features seen were anticipated. Many of the features are visually interesting, even beautiful at times. It is hoped that this new insight will help us reach the ultimate goal of the elimination of emitters.

REFERENCES

1. D.L. Moffat, et al., *Proc. 4th Workshop on RF Superconductivity*, KEK, Tsukuba, Japan, August 1989, 445. Also distributed as internal report CLNS 89-934, 1989.
2. J.R. Delayen and K.W. Shepard, *IEEE Trans. Mag.*, **27** (2), 1928 (1991).
3. Ph. Niedermann, N. Sankarraman, R.J. Noer and Ø. Fischer, *J. Appl. Phys.*, **59** (3), 892 (1986).
4. Ph. Niedermann, Ch. Renner, A.D. Kent and Ø. Fischer, *J. Vac. Sci. Technol.*, **A8** (1), 594 (1990).
5. R.H. Fowler and L. Nordheim, *Proc. Roy. Soc. Lond.*, **A119**, 173 (1928).
6. L.W. Nordheim, *Proc. Roy. Soc. Lond.*, **A121**, 626 (1928).
7. R.E. Burgess, H. Krömer and J.M. Houston, *Phys. Rev.*, **90** (4), 515 (1953).
8. R.H. Good and E.W. Müller, *Handbuch der Physik*, **XXI**, 176 (1956).
9. J. Halbritter, Institut für Material und Festkörperforschung, Kernforschungszentrum Karlsruhe, private communication.
10. B. Bonin, Departement de Physique Nucléaire, Centre d'études nucléaires de Saclay, private communication.
11. J. Graber, et al., to be published in Proc. 1991 IEEE Particle Accelerator Conference. Also distributed as internal report CLNS 91-1069, 1991.
12. J. Graber, et al., to be published in Proc. 5th SRF Workshop, DESY, Hamburg, Germany, August 1991. Also distributed as internal report CLNS 91-1105, 1991.
13. H. Piel, Fachbereich Physik, Bergische Universität Gesamthochschule Wuppertal, private communication.
14. R. Röth, Fachbereich Physik, Bergische Universität Gesamthochschule Wuppertal, private communication.
15. B. Rusnak, AT Division, Los Alamos National Laboratory, private communication.
16. C. Athwal and W. Weingarten, internal CERN report CERN/EF/RF 84-7 (1984).
17. E.L. Murphy and R.H. Good, Jr., *Phys. Rev.*, **102** (6), 1464 (1956).
18. Y.S. Touloukian and E.H. Buyco, *Specific Heat* (IFI Plenum, New York, 1970) Vol. 4, pp.153-156. (Data from curves 3, 4 and 5 were used.)
19. G.W. Webb, *Phys. Rev.*, **181** (3), 1127 (1969).
20. J-M Abraham, C. Tete and B. Deviot, J. Less-Common Metals, **37**, 181 (1974).
21. R. Hultgren, P.D. Desai, D.T. Hawkins, M. Gleiser, K.K. Keley and D.D. Wagman, *Selected Values of the Thermodynamic Properties of the Elements* (ASM, Metals Park, Ohio, 1973), pp. 336-341.
22. O. Kubaschewski and C.B. Alcock, *Metallurgical Thermochemistry* (Pergamon Press, Oxford, 1979), 5th ed.
23. H. Padamsee, et al., *Proc. 4th Workshop on RF Superconductivity*, KEK Tsukuba, Japan, August 1989, 207. Also distributed as internal report CLNS 89-937.
24. B. Jüttner, Physica, **114C**, 255 (1982).
25. E.A. Litvinov, G.A. Mesyats and D.I. Proskurovskii, *Sov. Phys. Usp.*, **26** (2), 138 (1983).
26. G.A. Mesyats, *IEEE Trans. Electrical Insulation*, **EI-18** (3), 218 (1983).
27. B. Jüttner, *IEEE Trans. Plasma Science*, **PS-15** (5), 474 (1987).
28. G.A. Mesyats and D.I. Proskurovsky, *Pulsed Electrical Discharge in Vacuum*, (Springer-Verlag, Berlin 1989), Chap. 5, pp. 106.
29. G.A. Loew and J.W. Wang, SLAC-Pub-4647 (1988). Presented at the XIIIth International Symposium on Discharges and Electrical Insulation in Vacuum, Paris, France, June 1988.
30. G.A. Loew and J.W. Wang, SLAC-Pub-5320 (1990). Presented at the XIVth International Symposium on Discharges and Electrical Insulation in Vacuum, Santa Fe, New Mexico, September 1990.
31. E.A. Litvinov, *IEEE Trans. Electrical Insulation*, **EI-20** (4), 683 (1985).
32. S.P. Bugaev, A.M. Iskol'dskii, G.A. Mesyats and D.I. Proskurovskii, *Sov. Phys.-Tech. Phys.*, **12** (12), 1625 (1968).
33. T.B. Massalski, J.L. Murray, L.H. Bennet and H. Baker, *Binary Alloy Phase Diagrams* (American Society for Metals, Metals Park, OH 1986).